

Modeling Non-stationary Tidal Processes
in the Lower Columbia River

Tobias Kukulka

Vordiplom, Physics, Freie Universität Berlin (1998)

A thesis presented to the faculty of the
OGI School of Science and Engineering
at Oregon Health and Science University
in partial fulfillment of the
requirements for the degree
Master of Science
in
Environmental Science and Engineering

May 2002

The thesis "Modeling Non-stationary Tidal Processes in the Lower Columbia River" by Tobias Kukulka has been examined and approved by the following Examination Committee:

Dr. David A. Jay, Thesis Advisor
Associate Professor, OGI School of Science & Engineering

Dr. António M. Baptista
Professor, OGI School of Science & Engineering

Dr. Patricia L. Toccalino
Assistant Professor, OGI School of Science & Engineering

Dr. Harry H. Yeh
Professor, University of Washington

Für Elfi, Matthias, Smail, Inge, Flo und Chris

Acknowledgements

I wish to express gratitude to my advisor Dr. David Jay for his persistent support, inspiration, and encouragement. I feel very thankful to David for making possible this thesis, while a fun and educational experience.

I would like to thank my other Committee Members, Dr. António Baptista, Dr. Patricia Toccalino, and Dr. Harry Yeh for their support of this work and for taking time to review and comment on this thesis.

I am thankful to my labmates Doug Wilson, Annika Fain, and Pradeep Naik. Special thanks go to Philip Orton, who endured "Die Fantastischen 4".

I would like to thank many OGI students and staff and all my friends in Berlin. I am thankful to my uncle Michael and my aunt Gabi for always being so encouraging.

I feel grateful to my parents Elfi, Matthias, Smail, and Inge, and my brothers Chris and Flo who have supported me throughout my life and who have always been there for me. Very special thanks are due to my girlfriend Jia who has morally supported me throughout graduate school.

This work was partially funded by the US Army Corps of Engineers and the National Oceanic and Atmospheric Administration, National Marine Fisheries Service, through a project entitled "Estuarine Habitat and Juvenile Salmon – Current and Historic Linkages in the Lower Columbia River and Estuary: Physical Oceanography Component". This work was also supported by the Department of Environmental Science and Engineering at the OGI School of Science & Engineering at OHSU.

Contents

Dedication.....	iii
Acknowledgements.....	iv
Contents.....	v
List of Figures.....	vii
List of Tables.....	ix
List of Symbols.....	x
Abstract.....	xiii
1 Introduction.....	1
2 Setting.....	4
2.1 <i>River Flow Variability</i>	4
2.2 <i>Tidal Processes</i>	5
3 Non-stationary Fluvial Tide Model.....	7
3.1 <i>Theory of Fluvial Tides</i>	7
3.2 <i>Bedstress</i>	9
3.3 <i>Analytic Solutions</i>	10
3.4 <i>Regression Model for Normalized Amplitude and Phase</i>	15
3.5 <i>Tidal Range</i>	18
3.6 <i>Overtide Properties</i>	19
4 Data Analysis Methods.....	22
4.1 <i>Continuous Wavelet Transform</i>	22
4.2 <i>Tidal Range Filter</i>	24

4.3 Data.....	25
5 Results and Discussion.....	27
5.1 Modulation of the Oceanic Tidal Frequency Spectrum.....	27
5.2 Model Coefficients.....	29
5.2.1 River Flow Coefficient.....	29
5.2.2 Neap-spring Coefficient.....	31
5.2.3 Geometry Coefficient.....	32
5.3 Reconstruction of D_2 , D_1 , Amplitudes and R	33
5.4 Phases.....	35
5.5 Overtides.....	36
6 Summary and Conclusions.....	37
References.....	38
Appendix A: Simplifications of Damping Modulus	73
Appendix B: First-order Relationship for Z_R.....	74
Appendix C: Note on Error Analyses.....	75
Biographical Sketch.....	83

List of Figures

1.1	Concept of tidal constituents, species, and stationarity.....	53
2.1	Watershed of the Columbia River.....	54
2.2	Changes in river flow variability.....	55
2.3	Location map showing stations in the Lower Columbia River	56
3.1	Conceptual model of tidal wave dissipation.....	57
3.2	Tschebyschev coefficients p_1, p_2 and p_3 and the integral P_3	58
5.1	Time series of surface elevation.....	59
5.2	Amplitude scaleograms.....	60
5.3a	Log-normalized D_2 and D_1 amplitude vs. river discharge.....	61
5.3b	Log-normalized R and D_4 amplitude vs. river discharge.....	62
5.3c	Log-normalized D_2 amplitude vs. river discharge at Cathlamet.....	63
5.4	River flow coefficient π_1	64
5.5	Neap-spring coefficient π_2	65
5.6	Geometry coefficient π_0	66
5.7a	Observed and modeled tidal amplitudes for D_2 and D_1	67
5.7b	Observed and modeled tidal amplitudes R and D_4	68
5.8a	Comparison of predictions for D_2 amplitudes at Columbia City.....	69
5.8b	Comparison of predictions for D_4 amplitudes at Columbia City.....	70
5.9	Flow coefficients for the D_2 and D_1 tidal wave number.....	71
5.10	Phase delays of diurnal and semidiurnal tidal waves	72
Ap.1a	D_2 amplitude bias analysis.....	77
Ap.1b	D_2 amplitude error analysis	78
Ap.2a	D_1 amplitude bias analysis.....	79
Ap.2b	D_1 amplitude error analysis.....	80

Ap.3a <i>R</i> amplitude bias analysis.....	81
Ap.3b <i>R</i> amplitude error analysis	82

List of Tables

1	Station-years available for tidal analysis.....	41
2	Average rms error for all stations from Jetty A to Vancouver.....	42
3	Ratio of D_4 phase coefficients to D_2 phase coefficients as function of position....	43
4a	Amplitude errors for D_2 , D_1 , and R using station-year specific coefficients.....	44
4b	Amplitude errors for D_2 , D_1 , and R using universal coefficients.....	45
4c	D_4 Amplitude errors.....	46
5a	Determined coefficients π_0 , π_1 , and π_2 for semidiurnal tidal amplitude.....	47
5b	Determined coefficients π_0 , π_1 , and π_2 for diurnal tidal amplitude.....	49
5c	Determined coefficients π_0 , π_1 , and π_2 for tidal range.....	51

List of Symbols

Latin Symbols

A	channel cross-section, m^2
b	channel width, m
B	complex constant determined by boundary conditions
c_0	inviscid wave speed, ms^{-1}
$c_{1,2}$	constant coefficients
c_D	drag coefficient
D_1	diurnal tidal amplitude, m
D_1	diurnal tidal species
D_2	semidiurnal tidal amplitude, m
D_2	semidiurnal tidal species
D_4	quarter-diurnal tidal amplitude, m
D_4	quarter-diurnal tidal species
f	$D_1 - D_2$ interference factor, dimensionless
g	gravitational acceleration = $9.81ms^{-2}$
h	mean channel depth, m
H	depth scale equal to 10m
i	square root of -1
i	subscript index
K_1	luni-solar diurnal tidal constituent (period: 23.93h)
M_2	principal lunar tidal constituent (period: 12.42h)
N_2	larger lunar elliptic tidal constituent (period: 12.66h)
O_1	principal lunar diurnal tidal constituent (period: 25.82h)
P_1	principal solar diurnal tidal constituent (period: 24.07h)
p_i	coefficient of Tschebyshev polynomial, $i=0,1,2,3$

$P(u_R, u_T)$	linearized Tschebyshev polynomial
q	complex wave number, m^{-1}
Q	cross-sectionally water transport, m^3s^{-1}
Q_R	River flow transport, m^3s^{-1}
r	damping modulus, m^{-1}
R	tidal range, m
R	friction coefficient, $R = c_D U_s / (H \pi) P(u_R, u_T)$
S_2	principal solar tidal constituent (period=12.00h)
t	time, s
T	bed stress divided by water density, m^2s^{-2} .
U_s	scaling amplitude, equal to inviscid wave speed
U_T	tidal flow amplitude, ms^{-1}
U_T	tidal flow, ms^{-1}
U_R	river flow, ms^{-1}
x	along channel distance in m; $x = 0$ at estuary entrance, x increases landward
\bar{X}	$= \left(1, U_R, \frac{ z_0 ^2}{\sqrt{U_R}} \right)$ regression input vector
y	filter output
z	tidal surface elevation, m
z_0	tidal amplitude of incoming ocean tides, m
Z	log-normalized tidal amplitude, dimensionless

Greek Symbols

β	ratio of diurnal to semidiurnal amplitudes at ocean entrance, dimensionless
γ	phase angle between diurnal and semidiurnal wave, radian
$\Delta\phi$	phase difference, radian
ε	ratio of tidal amplitude to water depth, dimensionless
κ	wave number, m^{-1}
λ	D_4 response delay to D_2 forcing, radians

π_0	offset coefficient (geometry coefficient for amplitudes)
π_1	river flow coefficient
π_2	neap-spring tidal coefficient
$\bar{\pi}$	$= (\pi_0, \pi_1, \pi_2)$ amplitude coefficients
$\bar{\pi}'$	$= (\pi_0', \pi_1', \pi_2')$ phase coefficients
φ	tidal phase, radian
ω	tidal frequency, s^{-1}

Functions and Operators

$\text{abs}(\cdot)$	absolute value of complex number, see also $ \cdot $
$\text{arg}(\cdot)$	argument of complex number
$\text{conj}(\cdot)$	complex conjugate of complex number
$\text{exp}(\cdot)$	natural exponential
$\text{im}(\cdot)$	imaginary part of complex number
$\text{log}(\cdot)$	natural logarithm
$\text{re}(\cdot)$	real part of complex number
\bullet	matrix multiplication
\bar{X}^T	transpose of \bar{X}
$ \cdot $	absolute value of complex number, see also $\text{abs}(\cdot)$
$*$	convolution operator

Abstract

Modeling Non-stationary Tidal Processes in the Lower Columbia River

Tobias Kukulka

M.S., OGI School of Science and Engineering of Science and Technology

May 2002

Supervising Professor: David A. Jay

This investigation applies non-stationary time-series analysis methods and the St. Venant equations to model tidal range, tidal species amplitudes and phases of water surface elevation in the Lower Columbia River in reach from the ocean entrance to Bonneville Dam, 234 km upriver. To incorporate the non-stationary frictional effects of variable river discharge into a tidal model, the tidal wave is decomposed into tidal species, under the assumption that species properties vary slowly relative to a tidal period. The one-dimensional tide model, based on analytic wave solutions to the linearized St. Venant equations, uses six coefficients per tidal species to represent the upstream evolution of the frictionally damped tidal wave. The form of the coefficients is derived from the St. Venant equations, but their values are determined objectively from the data. About 50 station-years of surface elevation data collected (1981–2000) below Bonneville Dam were processed with a wavelet filter bank to retrieve time-series of tidal species properties. A min-max filter was used to estimate daily tidal range. Tidal range, diurnal, and semidiurnal amplitudes were predicted with root mean square errors < 30

mm. Thus, non-stationary fluvial tidal properties were modeled with a previously unattained level of compactness and accuracy. Future use of this model, together with a low-frequency river stage model, will include the reconstruction of historical water levels in the Lower Columbia River. These can be used in efforts to restore salmon habitat in the Columbia River below Bonneville Dam.

1 Introduction

Populations of Columbia River basin salmon have diminished to a small fraction of their former diversity and abundance [Bottom *et al.*, 2001]. Traditionally, assessments of the reason for the decline in salmon populations have focused on obvious habitat changes upriver of the most seaward dam at Bonneville, 235 km from the ocean. Simenstad *et al.* [1984, 1990] and Independent Scientific Group [1999] indicate, however, the fundamental importance of tidal-fluvial and estuarine processes to salmonids. Despite its significance, relatively little attention has been paid to the tidal-fluvial portion of the system between Bonneville and the upstream limits of salinity intrusion at about river km (rkm) 15 to 30. In this portion of the system, hereafter referred to as the Lower Columbia River (LCR), marsh, freshwater swamp, and seasonal floodplains are present [Thomas, 1983]. These shallow-water habitats not only supply organic matter to the estuary [Sherwood *et al.*, 1990], but also provide migrating juvenile salmon with food resources, protection from predators, and an opportunity to prepare for the transition to marine conditions [Bottom *et al.*, 2001].

The availability of tidal-fluvial, shallow-water habitat in the LCR depends on the distribution of riverbed elevation (the hypsometric curve), river stage and tidal range. Dredging, filling, and dike-construction since the late 19th century have significantly decreased shallow-water habitat area [Thomas, 1983]. Also, climate change, flow regulation, and irrigation diversion have changed the magnitude and shape of the annual flow hydrograph, reducing peak flow by an average of >40% and peak river stage by 0.5 up to 2.0 m during the spring and summer migration of juvenile salmonids [Bottom *et al.*, 2001]. Because of the frictional interaction of river flow and tidal range, decreased spring-summer flows have increased tidal range by an amount that has not previously been quantified. Thus, there is a need to assess the impacts of historical changes in both tidal range and river stage in the LCR.

This study is the first part of a two-part investigation, focusing on the effects of historical changes in Columbia River (CR) discharge on stage, tidal range, and the availability of shallow-water habitat in the LCR. In order to determine the dependence of water surface elevation on river flow, we decompose water levels into low-frequency river stage and tidal variations. The objective of this study is to develop a non-stationary tidal model that captures, in a simple form, non-linear interactions of variable discharge and ocean tidal forcing. (See Fig. 1.1 for the clarification of "non-stationary tides", "tidal species", and "neap-spring tides") In a future study, a river stage model will be developed, which enables, together with the tidal model from this study, the reconstruction of historical water levels and assessment of their impacts on the availability of shallow-water habitat.

We seek a representation of river tides that is, like harmonic analysis, extremely compact, yet powerful in its ability to hindcast or (with knowledge of river flow) predict tides. Existing tidal prediction methods (analytical models and harmonic analyses) are not suitable tools for our analyses of non-stationary tides. Both involve the assumption of stationarity of each tidal constituent (Fig. 1.1), which is invalid when tides interact with variable river flow, as is the case for the LCR [Godin, 1984; Jay and Flinchem, 1997]. Although considerable success has been achieved in modeling non-stationary tides numerically [Baptista *et al.*, 1999; Salerno and Markman, 1991], a simple closed-form prediction method is not a likely result.

Our tidal model applies wavelet transform tidal methods [Flinchem and Jay, 2000] and the dynamical model of Jay [1991] to analyze the non-stationary effects of variable river flow on tides. The dynamical model of Jay [1991] is an analytic solution to the linearized St. Venant equations, which incorporates frictional effects of river discharge due to bottom stresses. Our approach is valid as long as tidal amplitudes and phases vary slowly relative to the tidal period, a condition usually satisfied in the LCR. Further, in wavelet tidal analysis, a tidal wave is composed of tidal species (but not into constituents within tidal species, see Fig. 1.1), as is also done in the species concordance method [Simon, 1991]. Both the wavelet and species concordance approaches rely on the nonlinear relationships between tidal species at an analysis station and at another

reference station where the tide is well known and nearly stationary. Though the species concordance method is applicable to the interaction of tides with variable river flow, this method has several disadvantages and is therefore not used. First, it is necessary to take into account all possible combinations of tides and flow, requiring the analysis of long data records. Second, the method does not use knowledge of tidal wave dynamics, so that the dependence of a tidal species at an upriver location upon tidal properties of a reference station can only be expressed in polynomial terms. Finally, the determination of tidal species properties relies on a least square fit, with questionable results for strongly non-stationary records [*Jay and Flinchem, 1999*].

Analyses of the non-linear interactions of river flow and neap-spring tidal forcing provides a simple model of the spatial evolution of tidal properties. This model is compact and very efficient in predicting tidal species properties and tidal range. Our study offers a new vision for the prediction of riverine tides and is, thus, a response to Godin's recent conclusion: "Improved predictions [of river tides] will become possible when more careful consideration is given to fluctuations in river discharge, implying that short-time predictions should be considered, not conventional tide tables" [*Godin, 1999*].

2 Setting

The CR has the second greatest annual river discharge in western North America, with an average discharge of $\sim 7,500 \text{ m}^3 \text{ s}^{-1}$ [Sherwood *et al.*, 1990]. The drainage basin encloses an area of $660,500 \text{ km}^2$, and includes two subbasins (Fig. 2.1). The Interior Subbasin drains a large and mostly arid landscape, including parts of the Cascade Mountains, the Rocky Mountains in the United States and Canada, and the interior Ranges of British Columbia. The Coastal Subbasin drains high-precipitation terrain in Oregon and Washington west of the Cascade Mountains, including part of the Oregon Coast Range. Although the Coastal Subbasin includes only 8% of the total surface area, it contributes roughly 25% to the total CR flow [Sherwood *et al.*, 1990]. The tidal-fluvial section of the CR system below Bonneville Dam is included within the coastal sub-basin.

2.1 River Flow Variability

There are three characteristic time scales of non-tidal CR freshwater flow variation: 1) interannual and lower frequency, 2) seasonal, and 3) daily and weekly variations caused by fluctuations in electric power demand ("power peaking"). Interannual and lower frequency flow fluctuations are related to climatic changes [Latif *et al.*, 1994] and play a major role in the habitat investigation. CR flows over the last 140 years show both interdecadal variability (the Pacific Decadal Oscillation [Mantua *et al.*, 1997]) and a long-term decrease in river flow [Bottom *et al.*, 2001]. Although irrigation depletion is responsible for part of the decline in river flow, the impact of long-term climate change is of equal magnitude [Sherwood *et al.*, 1990; Bottom *et al.*, 2001]. Before flow regulation, annual maximum discharge was usually observed during May-July freshet periods, due to snowmelt mainly in the Interior Subbasin. Transient winter high-flow events occur when heavy snowmelt and rainfall in the western subbasin accompany

warm and intense storms. During November to March river flow may fluctuate on time scales of days to weeks. Flow regulation and climate warming have increased winter flows to the point where they now sometimes exceed those during spring freshets.

Flow regulation also now causes spring freshet flows to follow a different time history than they would in the absence of flow regulation (Fig. 2.2) [Sherwood *et al.*, 1990]. Reservoir storage (amounting to ~60% of mean annual flow volume) has greatly reduced spring freshet amplitude, increased fall and winter flows, decreased seasonal flow variability, and spread flows from the largest freshets into the subsequent year (Fig. 2.2). The maximum daily mean flows during the spring freshets have been reduced by an average of $9,500 \text{ m}^3\text{s}^{-1}$, and now seldom exceed $16,000 \text{ m}^3\text{s}^{-1}$ [Bottom *et al.*, 2001].

Finally, an irregular daily power-peaking cycle introduces a pseudo-diurnal tide, propagating seaward from Bonneville Dam at rkm-234. The power-peaking cycle also exhibits weekly fluctuations due to lower power demand on weekends. Power peaking is often suppressed during high-flow periods, because water is spilled when power demand drops. Power-peaking fluctuations propagate as waves [Wiele and Smith, 1996], but differ from tides in that they are broadband, not band-limited, signals. All these annual changes in flow cycle have an impact on the tidal properties of the LCR.

2.2 Tidal Processes

The tidal range in the LCR is 1.7 to 3.6 m at the ocean entrance and increases to a maximum between 2.0 and 4.0 m, at Astoria (rkm-29) [Jay, 1987]. It then decreases in the landward direction to <0.2 m above Vancouver at rkm-171 [Jay, 1987]. The tide has a mixed character with a ratio of semidiurnal to diurnal amplitude of 1.5 at the estuary mouth [Jay, 1987]. CR tides are quite non-stationary landward of rkm-30, so that a description of mean properties in terms of tidal constituents is an approximation, but still a useful one. The principal lunar component (M_2) increases from 0.82 m at the mouth of the river to 0.95 m at Tongue Point (Fig. 2.3) during low flow season, and then steadily decreases landward [Jay, 1984]. The lunar-solar component (K_1) is nearly constant at 0.4 m over the lower 30 km, before landward damping occurs [Jay, 1984]. Tidal propagation in the main channel is weakly non-linear with respect to depth fluctuation, since the

amplitude to depth ratio is ~ 0.1 in the estuary and decreases thereafter [Jay, 1984]. Non-linear tidal interactions (self-damping) generate even overtides. The ratio of M_2 to its first overtide, M_4 , is 30 to 50 in the lower estuary, and decreases to 3 to 10 in the tidal river [Giese and Jay, 1989]. There is an abrupt 180° phase change in M_4 at rkm-35, suggesting that strong river flow dominates fluvial overtide generation landward of this point, whereas the incoming ocean wave and frictional effects associated with tidal flats are important in the estuary [Jay and Musiak, 1996].

Following Jay *et al.* [1990] the energy budget for the LCR exhibits three reaches: a) the tidally dominated lower estuary from the ocean entrance up to \sim rkm-15; b) an intermediate, dissipation-minimum between rkm 15 and 50; and c) a tidal-fluvial reach landward of rkm-50. In the first regime, energy for circulation is derived primarily from barotropic tides. Both tidal and fluvial energy are important in the second reach, although dissipation remains small. The upstream limits of salinity intrusion and a long-term locus of deposition are found in the dissipation-minimum region [Giese and Jay, 1989]. Dissipation in the tidal river is derived mainly from the river flow. Our analysis separates the reach landward of rkm-140 from the rest of the tidal-fluvial reach. In this part of the system, the tidal frequency spectrum is also modified by hydroelectric power peaking.

3 Non-stationary Fluvial Tide Model

The strategy employed here to describe CR fluvial tides is to use analytical solutions to model the dependence of tidal amplitude and phase on upriver location and river flow. The model coefficients for each species are determined by regression analysis to optimize the prediction power of the model. The spatial pattern of the coefficients is consistent between species and yields a clear physical interpretation.

3.1 Theory of Fluvial Tides

The distinct and complex motion of riverine tides [see e.g. *Godin, 1984*] as a result of the interaction among tidal species and freshwater discharge can be understood by the analysis of the governing St. Venant equations:

$$\frac{\partial Q}{\partial t} + \frac{\partial}{\partial x} \left(\frac{Q^2}{A} \right) + gA \frac{\partial z}{\partial x} + bT = 0 \quad (3.1.1a)$$

$$\frac{\partial Q}{\partial x} + b \frac{\partial z}{\partial t} = 0 \quad (3.1.1b)$$

where

x along channel distance in m; $x = 0$ at estuary entrance, x increases landward

t time, s

$z(x,t)$ water surface elevation, m

$Q(x,t)$ cross-sectionally integrated water transport, $m^3 s^{-1}$

z and Q are complex numbers

$A(x, Q_R) = b h$	channel cross-sectional area, m^2
$b(x, Q_R)$	channel width, m
$h(x, Q_R)$	mean channel depth, m
Q_R	cross-sectionally integrated river flow transport, m^3s^{-1}
g	gravitational acceleration = $9.81ms^{-2}$
T	bed stress divided by water density, $T = c_D U U$, m^2s^{-2} .
c_D	drag coefficient, $\approx 3 \cdot 10^{-3}$
U	flow velocity, ms^{-1}

The cross-sectionally integrated momentum equation (3.1.1a) indicates that the local acceleration (first term from left) is due to the convective acceleration (second term), water surface slope (third term), and friction (fourth term). The cross-sectionally integrated continuity equation (3.1.1b) shows along-channel changes in water transport are balanced by temporal changes in water surface elevation. Equations (3.1.1a) and (3.1.1b) together suggest that the propagation of a tidal wave is determined by the balance of inertia, friction and topography. With slowly varying cross-sectional channel area and in the absence of friction, gravitational forces balance local acceleration, resulting in a dynamic wave [Lamb, 1932]. Energy flux is conserved, and Green's Law applies. Green's Law relates tidal amplitude inversely to b and h as $b^{-1/2}h^{-1/4}$ [Green, 1837]. In most estuaries, however, friction and topographic funneling cause the tidal wave to deviate from a dynamic wave. The LCR geometry is divergent from the ocean entrance to rkm-11, convergent up to rkm-50, and weakly convergent thereafter [Giese and Jay, 1989]. Following Seminara and Lanzoni [1998], the LCR as a whole can be classified as a "Strongly Dissipative and Weakly Convergent" estuary, which is similar to the Jay [1991] "critical convergence" regime. In this regime inertia is negligible, which causes tidal propagation to approach a diffusive condition, as in the Fraser River and many other river estuaries [LeBlond, 1978; Jay, 1991]. Friedrichs and Aubrey [1994] showed that tidal wave distortion in a strongly convergent channel can be approximately described by a first-order differential equation, but the "critical convergence" regime is more realistic for the CR, where channel cross-section convergence rate is small landward of rkm-50.

3.2 Bedstress

A key point in modeling frictional effects on tides is the representation of the bedstress, which is responsible for the dissipation of tidal energy (see also Fig. 3.1). Many researchers [see e.g. *Godin*, 1991] have noticed that the bedstress law

$$T = c_D U|U| \quad (3.2.1)$$

approximates an odd function in U for oscillatory flow, even though the dependency of T on U appears to be "quadratic". Because of this character, the bedstress is often represented [see e.g. *Godin*, 1991] in the form

$$T \approx \text{const}_1 U + \text{const}_2 U^3 \quad (3.2.2)$$

where const_1 and const_2 are constants chosen to fit $c_D U|U|$. When, however, strong river flow is present, as in the CR, the expansion in odd powers becomes inadequate. This is evident for the case in which river flow is stronger than tidal flow, so that the current never reverses. Then $U|U| = U^2$ is an even function. The Tschebyschev polynomial approach [*Dronkers*, 1964] takes into account this change from an odd to an even function, with increasing zero-frequency flow. It provides, thus, an intuitively appealing explanation of the change in character of tidal interaction with river flow. Following *Dronkers* [1964], T can be represented as:

$$T \approx c_D (p_0 U_s^2 + p_1 U_s U + p_2 U^2 + p_3 U^3 / U_s) / \pi \quad (3.2.3)$$

where U_s is a flow scale that is determined by the average of the absolute values of U_{\max} and U_{\min} during a tidal period and p_i , $i=0,1,2,3$ are the Tschebyschev coefficients, which depend on the ratio of tidal current amplitude U_T to river flow currents U_R (see also Fig. 3.2). For $U_T < U_R$, $p_0 = p_1 = p_3 = 0$ and $p_2 = \pi$, so that $T = c_D U^2$, as expected. If U_R approaches zero, $p_0 = p_2 = 0$, $p_1 = 16/15$, and $p_3 = 32/15$, so that (3.2.3) is an odd function. Effects of T in (3.1.1a) can be intuitively understood by substituting $U = U_T + U_R$ into

(3.2.3), where U_T and U_R are cross-sectionally averaged tidal and river flow velocity, respectively. For simplicity, we retain only the dominant second and third terms and omit the first and fourth terms to obtain:

$$T = (p_1 U_s U_R + p_2 U_R^2 + p_1 U_s U_T + p_2 U_T^2 + 2 p_2 U_T U_R) / \pi \quad (3.2.4)$$

The first two terms on the right hand-side are zero-frequency and do not directly contribute to the tidal momentum balance. The third term represents linear self-damping of the tide. The last term suggests that more tidal energy dissipates for greater river flow. The fourth term shows that the bedstress term is also responsible for the generation of overtides, which can be seen as follows. For simplicity let $U_T = U_T \cos(\omega_{D2} t)$, where ω_{D2} is the semidiurnal tidal frequency. Now, using a simple trigonometric theorem of addition, we find that $U_T^2 = U_T^2 / 2 [1 + \cos(2\omega_{D2} t)]$, so that damping of semidiurnal tidal energy generates not only dissipative energy loss, but also a quarterdiurnal wave ($2\omega_{D2}$ is a quarter-diurnal frequency) and a zero-frequency component ("1" is zero-frequency).

The Tschebyschev polynomial bedstress representation can be used to derive an analytical solution to the St. Venant equations [Jay, 1991]. Because of the Tschebyschev polynomial approach provides a realistic bedstress treatment for a wide range of the U_T/U_R rates, as appropriate for the LCR system, we follow this approach in our analysis.

3.3 Analytic Solutions

To derive a solution to (3.1.1a) and (3.1.1b), we decompose the water transport Q into a low-frequency part Q_R and a tidal part Q_T , so that

$$Q = Q_R + Q_T \quad (3.3.1)$$

and substitute (3.3.1) for Q into (3.1.1a) and (3.1.1b). Now we expand (3.1.1a) and (3.1.1b) in the small perturbation parameter, the ratio of tidal amplitude to depth $\varepsilon = |z|/h$.

Keeping only lowest and first-order terms and sorting by dominant tidal frequency we obtain for the momentum equation (3.1.1a)

$$\frac{\partial Q_T}{\partial t} + 2U_R \frac{\partial Q_T}{\partial x} - 2U_R \frac{d[\ln(A)]}{dx} Q_T + gA \frac{\partial z_T}{\partial x} + (bT)_T = 0 \quad (3.3.2a)$$

where U_R is the river flow velocity or Q_R/A . The continuity equation has the form

$$\frac{\partial Q_T}{\partial x} + b \frac{\partial z_T}{\partial t} = 0 \quad (3.3.2b)$$

The subscript T indicates a tidal variable and will be dropped, however, for simplicity, thus $Q_T \rightarrow Q$, $z_T \rightarrow z$ and $(bT)_T \rightarrow bT$. To solve for Q and z , we cross-differentiate, i.e. take the time derivative of the momentum equation (3.3.2a) divided by (gh) :

$$\frac{1}{gh} \frac{\partial^2 Q}{\partial t^2} + 2 \frac{1}{gh} U_R \frac{\partial^2 Q}{\partial x \partial t} - 2 \frac{1}{gh} U_R \frac{d[\ln(A)]}{dx} \frac{\partial Q}{\partial t} + b \frac{\partial^2 z}{\partial x \partial t} + \frac{b}{gh} \frac{\partial T}{\partial t} = 0 \quad (3.3.3a)$$

and the spatial derivative of the continuity equation (3.3.2b):

$$\frac{\partial^2 Q}{\partial x^2} - \frac{d[\ln(b)]}{dx} \frac{\partial Q}{\partial x} + b \frac{\partial^2 z}{\partial x \partial t} = 0 \quad (3.3.3b)$$

Subtraction of (3.3.3a) from (3.3.3b) results in the governing wave equation:

$$\frac{\partial^2 Q}{\partial x^2} - \frac{d[\ln(b)]}{dx} \frac{\partial Q}{\partial x} - 2 \frac{1}{gh} U_R \frac{\partial^2 Q}{\partial x \partial t} + 2 \frac{1}{gh} U_R \frac{d[\ln(A)]}{dx} \frac{\partial Q}{\partial t} - \frac{1}{gh} \frac{\partial^2 Q}{\partial t^2} - \frac{b}{gh} \frac{\partial T}{\partial t} = 0 \quad (3.3.3c)$$

The terms from left to right are due to the pressure gradient, pressure gradient and topography, convective accelerations (two terms), local acceleration, and bed stress. We

formed here the wave equation in Q , rather than in z , because the bedstress representation is simpler expressed in Q . Once a solution to Q is determined, z is calculated from the continuity equation (3.3.2b). This formulation and its approximate solution below use the following assumptions:

- a) *Transport*: The tidal transport Q is one-dimensional in x .
- b) *Geometry*: The channel geometry is straight, time-independent, and exponentially converging in depth and width, although the convergence rate is a function of x . The effects of tidal flats, bifurcations, and islands are neglected, though they are quite prominent in the first 50 rkm.
- c) *River Flow*: River flow enters only at one source and varies slowly relative to the tides. This is fulfilled to lowest order, although power-peaking cycles at Bonneville Dam and river flows from the Willamette River (rkm-165) and other tributaries can cause occasional violations of this assumption.
- d) *Forcing Mechanisms*: Effects of wind stresses and baroclinic forcing are negligible. Both are significant forcing mechanisms in the estuary but are small further landward [Jay, 1987; Jay and Musiak, 1996].
- e) *Interactions of Tidal Species*: It is assumed that each tidal species can be treated in isolation, aside from damping of the diurnal wave (D_1) by the semidiurnal wave (D_2), and frictional generation of overtides by both D_1 and D_2 .

To obtain an analytical solution, we still need to represent the bedstress term T (3.2.1) in a tractable form. This can be achieved by using *Dronkers* [1964] bedstress approach as discussed in the previous section. Again, we represent T in terms of tidal and low-frequency velocity and consider only the terms having the frequency of a particular tidal species in the wave equation for that species. By neglecting small amplitude effects, the bedstress takes the form:

$$T = Q R/b \quad (3.3.4)$$

where

$$R = c_D U_s / (H \pi) P(u_R, u_T) \quad (3.3.5a)$$

$$P \cong p_1 + p_2 u_R + p_3 \left(3u_R^2 + \frac{1}{2} u_T^2 \right) \quad (3.3.5b)$$

with

u_T amplitude of tidal velocity (scaled with U_s), dimensionless

u_R river flow velocity (scaled with U_s), dimensionless

H depth scale equal to 10m

For further details on this linearization procedure we refer to *Jay* [1991], (22).

Substituting the linearized bedstress into (3.3.3c), we need to solve the following wave equation:

$$\frac{\partial^2 Q}{\partial x^2} - \frac{d[\ln(b)]}{dx} \frac{\partial Q}{\partial x} - 2 \frac{1}{gh} U_R \frac{\partial^2 Q}{\partial x \partial t} + 2 \frac{1}{gh} U_R \frac{d[\ln(A)]}{dx} \frac{\partial Q}{\partial t} - \frac{1}{gh} \frac{\partial^2 Q}{\partial t^2} - \frac{R}{gh} \frac{\partial Q}{\partial t} = 0 \quad (3.3.6)$$

It is then necessary to separate the dependence of Q and z on the variables t and x and to assume an oscillatory time dependence of Q , so that

$$Q(x, t) = \bar{Q}(x) \exp(i\omega t) \quad (3.3.7)$$

For sake of intuition, let us neglect the convective acceleration terms as small and assume that the width and depth do not vary with x ; (3.3.6) then becomes

$$\frac{\partial^2 Q}{\partial x^2} - \frac{1}{gh} \frac{\partial^2 Q}{\partial t^2} - \frac{R}{gh} \frac{\partial Q}{\partial t} = 0 \quad (3.3.8)$$

Substituting (3.3.7) for Q gives:

$$\overline{Q}'' + \frac{\omega^2 \overline{Q}}{hg} - \frac{i\omega R}{hg} \overline{Q} = 0 \quad (3.3.9)$$

where " indicates the second derivative with respect to x . If \overline{Q} is specified as

$$\overline{Q} = B \exp(-iqx) \quad (3.3.10)$$

where q is the complex wave number and B a constant coefficient determined from the boundary conditions, we obtain the following characteristic equation:

$$-q^2 + \frac{\omega^2}{hg} \left(1 - \frac{iR}{\omega} \right) = 0 \quad (3.3.11)$$

with its solution for an incident wave

$$q = \frac{\omega}{\sqrt{hg}} \sqrt{1 - \frac{iR}{\omega}} = \kappa - ir \quad (3.3.12)$$

where

κ $\text{re}(q)$, wave number, m^{-1}

r $\text{im}(q)$, damping modulus, m^{-1}

Eq. (3.3.7) to (3.3.12) allow the following physical interpretation. If inertia is dominant (for $\omega \gg R$) κ is approximately real, and the wave speed converges to the inviscid limit $\omega/\kappa = (gh)^{1/2}$. If friction is present, the wave number is complex, so that the tidal height and transport is exponentially damped with x . Inertia is negligible for large R (relative to ω , $R \gg \omega$), so that the real and imaginary part of q are equal, and the resulting wave is diffusive [LeBlond, 1978; Jay, 1991]. In this case we have

$$\kappa = -r = \frac{1}{\sqrt{gh}} \sqrt{\frac{R\omega}{2}} \quad (3.3.13)$$

If the channel geometry is dependent on x , the propagating wave is topographically funneled. For an analytical solution, we need to transform the wave equation to obtain a differential equation with constant coefficients. This can be achieved by changing the independent variable x , so that an inviscid (zero friction) wave travels equal distance in equal times regardless of depth [Jay, 1991]. The dependent variable is changed in order to obtain the following solution for the incident tidal wave of height z :

$$z(x,t) = z_0 \operatorname{Re} \left(\sqrt{\frac{A(0)}{A(x)}} \exp(i\omega t - iqx) \right) \quad (3.3.14)$$

where $z_0 = z_0(t) = |z(0,t)|$ is the tidal species amplitude of the incoming ocean tide and q is the complex wave number defined above in (3.3.13). Jay [1991] termed this the "critical" solution in which effects of convergence and inertia approximately balance each other and friction dominates the wave number. In our implementation of (3.3.14), small corrections to the wave number due to river flow (implicit in 3.3.6) are neglected. The boundary conditions are: a) the amplitude and phase are known at the estuary mouth, and b) the wave vanishes for large x , so that the reflective wave is absent. Using this solution, we develop a simple regression model applicable to each tidal species.

3.4 Regression Model for Normalized Amplitude and Phase

Practical application of the above model requires manipulation of (3.3.5, 3.3.13-14) into a form allowing a regression analysis to determine the spatial variation of the p_i , $i=1,2,3$, for each station and species. Each species is assumed harmonic (3.3.7) despite the sub-tidal evolution of the wave (due to variable river flow) with amplitude $|z|$ and phase φ . It is also convenient to eliminate variations caused by changes in ocean forcing. This is accomplished by normalizing $|z|$ and φ by the incoming ocean tide, to obtain the log-normalized amplitude Z and phase difference $\Delta\varphi$ at any location in the river channel:

$$Z(x) = \log\left(\frac{|z(x,t)|}{|z(0,t)|}\right) = \frac{1}{2} \log\left(\frac{A(0)}{A(x)}\right) + rx \quad (3.4.1a)$$

$$\Delta\varphi(x) = \arg(z(x,t)) - \arg(z(0,t)) = -\kappa x \quad (3.4.1b)$$

Note that, according to (3.3.14), $|z(x,t)| = z_0 \sqrt{A(0)/A(x)} \exp(rx)$ and $|z(0,t)| = z_0$.

Z and $\Delta\varphi$ should be related to river flow and the frictional (non-linear) effects of ocean tidal forcing through R . To find the simplest and most physical linear regression model, we examine more closely the damping modulus $r = -\kappa$ (see Appendix A):

$$\begin{aligned} r &= \frac{-1}{c_0} \sqrt{\frac{c_D U_s \omega}{2H\pi}} \left[p_1 + p_2 u_R + p_3 \left(3u_R^2 + \frac{1}{2} u_T^2 \right) \right]^{\frac{1}{2}} \\ &\approx c_1' u_R + c_2' \frac{u_T^2}{\sqrt{u_R}} \approx c_1' u_R + c_2' \left(\frac{c_0}{h} \right)^2 \frac{z_0^2}{\sqrt{u_R}} \end{aligned} \quad (3.4.2)$$

where $u_T \approx z_0 / h$ for a linear incident wave, $z_0 = z_0(t) = |z(0,t)|$, and $c_0 = (gh)^{1/2}$.

The coefficients c_1' and c_2' arise from the first-order approximations in (3.4.2) (see Appendix A). Both coefficients are proportional to the square root of the tidal frequency and vary with U_R/U_T . To lowest order, c_1' and c_2' are proportional to p_2 and p_3 , respectively. If the coefficients π_1 , π_2 , and π_0 are defined as:

$$\pi_1(x) = c_1' x \quad (3.4.3a)$$

$$\pi_2(x) = c_2' x \left(\frac{c_0}{h} \right)^2 \quad (3.4.3b)$$

$$\pi_0(x) = \frac{1}{2} \log\left(\frac{A(0)}{A(x)}\right) \quad (3.4.3c)$$

the log-normalized amplitude Z can be modeled linearly in the parameters π_0, π_1, π_2 , using U_R and z_0 as the only input variables. The coefficients π_1 and π_2 determine the exponential damping rate and phase delays in x of the dominant tidal species. Frictional damping and phase delays through river discharge is mainly captured by the "river flow" coefficient π_1 , while the "neap-spring" coefficient π_2 reflects the fact that frictional damping and phase delay depend non-linearly on the amplitude of incoming ocean tides. The "geometry" coefficient π_0 captures topographic funneling as function of x . The Tschebyshev coefficients are functions of the ratio of tidal flow amplitude to river flow, and since this ratio changes with upriver distance, π_1' will not vary linearly with x , but a physically meaningful pattern emerges from the analysis below.

If we also assume a linear offset π_0' in (3.4.1b) for $\Delta\varphi$ due to the simplifications made in (3.4.2), we have for Z and $\Delta\varphi$ for the dominant tidal species:

$$Z(x) \approx \bar{\pi} \bullet \bar{X}^T \quad (3.4.4a)$$

$$\Delta\varphi(x) \approx \bar{\pi}' \bullet \bar{X}^T \quad (3.4.4b)$$

where:

$\bar{\pi} = (\pi_0, \pi_1, \pi_2)$ amplitude coefficients

$\bar{\pi}' = (\pi_0', \pi_1', \pi_2')$ phase coefficients

$$\bar{X} = \left(1, U_R, \frac{|z_0|^2}{\sqrt{U_R}} \right)$$

• Matrix multiplication

\bar{X}^T Transpose of \bar{X}

The above model applies only to major tidal species. Thus, there is still a need to determine the behavior of the tidal range and overtides, as described in the following sections.

3.5 Tidal Range

Daily tidal range is estimated as the difference between maximum and minimum heights during one 12.42 h tidal period, with the fidelity of the estimate being dependent on the time resolution of the data. The mean tidal range is approximately twice the amplitude of the dominant tidal constituent, M_2 . The actual range, however, is dependent on the phases and amplitudes of all the larger constituents, as manifested in the grouping formula given by the US Coast and Geodetic Survey [1952, p.10]. Since major tidal constituents in the ocean (M_2 , S_2 , N_2 , K_1 , and O_1) are stationary, the tidal range near the estuary mouth can be easily predicted from harmonic properties. Further upriver, the tidal species interact through the bedstress with each other and with the variable river flow. This causes non-stationary tides, complicating significantly the analysis and prediction of the tidal range in the tidal fluvial part of the system.

A lowest order dependency of the range coefficients $\bar{\pi}_R$ on the semidiurnal and diurnal coefficients, $\bar{\pi}_{D_2}$ and $\bar{\pi}_{D_1}$ can be derived by approximating the log normalized tidal range Z_R as:

$$Z_R(x) \cong \log \left(\frac{|D_2(x)| + \cos(\gamma)|D_1(x)|}{|D_2(0)| + \cos(\gamma)|D_1(0)|} \right) \quad (3.5.1)$$

where $\gamma = \gamma(x)$ is the phase angle between the diurnal and semi-diurnal wave. For the lowest order estimate, we assume that the tidal range is only composed of the D_1 and D_2 wave. This is justified when estimating the daily maximum range over a tidal day, so that constructive superposition of D_1 and D_2 can take place. Setting now $D_1(0) = \beta D_2(0)$, where D_2 and D_1 are tidal amplitudes (in m) of the semidiurnal, diurnal tidal species respectively, and $f = \beta \cos(\gamma)$, where $0 < f < \beta$, we obtain the following approximation (see Appendix B):

$$Z_R(x) \cong \log \left(\frac{\exp(\bar{\pi}_{D_2} \bullet \bar{X}^T) + f \exp(\bar{\pi}_{D_1} \bullet \bar{X}^T)}{1 + f} \right) \\ \cong ((1 - f)\bar{\pi}_{D_2} + f\bar{\pi}_{D_1}) \bullet \bar{X}^T \quad (3.5.2)$$

for $f \ll 1$. From this derivation we estimate the following lowest order value for the range coefficients:

$$\bar{\pi}_R = (1 - f)\bar{\pi}_{D_2} - f\bar{\pi}_{D_1} \quad (3.5.3)$$

Consequently, range can also be predicted using a formula like (3.4.1a). We expect the π_{Ri} to be between the coefficients of the major tidal species, but closer to the $\pi_{D_{2i}}$, than to the $\pi_{D_{1i}}$, $i = 0, 1, 2$. The influence of overtides causes some deviations from (3.5.2), which do not, however, interfere with the analysis based on (3.4.1a).

3.6 Overtide Properties

River flow effects on fluvial overtides are fundamentally different than effects on D_1 and D_2 because overtides are primarily generated, as well as damped, due to the frictional energy transfer between frequencies. For high river discharge, momentum transfer from D_2 to D_4 is due largely to the quadratic frictional interaction, rather than to convective acceleration [Parker, 1991]. The wave equation [equivalent to (3.3.3c)] for overtides is an inhomogeneous differential equation because of the forcing terms. Further upriver, where the incident oceanic quarter-diurnal wave (D_4) has lost most of its energy, the D_4 wave solution to (3.3.3c) is a forced wave with its amplitude also linear in $U_R |D_2|^2$ and $|D_2|^2$, and oscillating with $D_2^2 / |D_2|^2 \exp(i\lambda)$, where λ is a phase delay, due to the response delay to the forcing of the system. Sufficiently far upriver, we have:

$$D_4(x, t) \cong |D_4(x, t)| \exp(i[\omega_4 t - \kappa_4 x + \lambda]) \quad (3.6.1)$$

where

$$\omega_4 \approx 2 \omega_2$$

$$\kappa_4 \approx 2 \kappa_2 \quad (3.6.2)$$

$$|D_4| \quad \text{linear in } U_R |D_2|^2 \text{ and } |D_2|^2$$

Note that if the response delay λ is nearly independent of river flow and tidal range, the phase of D_4 can be modeled by analogy to (3.4.4). Then, the phase difference $\Delta\varphi_4 = \arg(D_4(x,t)) - 2 \arg(D_2(0,t))$ should lead to flow and neap-spring coefficients, so that

$$\pi_{i,D4} = 2 \pi_{i,D2}, \quad i = 1,2 \quad (3.6.3)$$

To determine if the phase response is really nearly independent of river flow, one can examine the forced wave equation. Examining the bedstress term (3.2.3) yields for the D_4 forcing component $T_{4,forcing}$ of the bedstress:

$$T_{4,forcing} = \frac{bc_D}{ghA^2} \left(p_2 + p_3 \frac{U_R}{U_s} \right) Q_2^2 \quad (3.6.4)$$

where the subscript "2" indicates a semidiurnal component and "4" a quarter-diurnal one. Let us specify the semidiurnal transport as:

$$Q_2(x,t) = |Q_2(x,t)| \exp(i[\omega_2 t - \kappa_2 x]) \quad (3.6.5)$$

Now, the forcing term $F(x,t)$ due to the semidiurnal wave in the wave equation (3.3.3c) is:

$$F(x,t) = \frac{\partial}{\partial t} T_{4,forcing} = i C Q_2^2, \quad \text{with } C = 2\omega_2 \frac{bc_D}{ghA^2} \left(p_2 + p_3 \frac{U_R}{U_s} \right) \quad (3.6.6)$$

If we use for the D_4 self-damping and fluvial parts of the bedstress the representation (3.3.4) and (3.3.5), and again neglect convective accelerations and the dependence of geometry on x , the forced wave equation has the form (compare to (3.3.8)):

$$\frac{\partial^2 Q_4}{\partial x^2} - \frac{1}{gh} \frac{\partial^2 Q_4}{\partial t^2} - \frac{R}{gh} \frac{\partial Q_4}{\partial t} = F(x, t) \quad (3.6.7)$$

To develop an intuition for this inhomogeneous differential equation let us assume a wave solution of the form:

$$Q_4(x, t) = B \exp(i[a_4 t - q_4 x]) \quad (3.6.8)$$

Substituting Q_4 in the forced wave equation (3.6.7) yields:

$$Q_4 = i \left\{ q_4^2 + \frac{\omega_4}{gh} \left(1 - \frac{iR}{\omega_4} \right) \right\}^{-1} C Q_2^2 \quad (3.6.9)$$

The response phase delay λ_Q of Q_4 relative to Q_2^2 forcing can now be written as

$$\lambda_Q = \arg \left(i \left\{ q_4^2 + \frac{\omega_4}{gh} \left(1 - \frac{iR}{\omega_4} \right) \right\}^{-1} \right) \quad (3.6.10)$$

Thus, since R and q_4 are functions of river flow [see (3.3.5)], our simple analysis suggests that λ is also a function of river flow. Consequently, (3.6.3) must be seen as a lowest order approximation. As long as the variation of λ is no more than linear with Q_R , however, the regression analysis will simply absorb this variability into π_{1D4}' .

Similarly, simple forced wave solutions like (3.6.1) can be obtained for other overtides, which are, however, not discussed here. In the next section we introduce to the methodology necessary to extract D_1 , D_2 , D_4 , and R properties from tidal height data.

4 Data Analysis Methods

Tidal damping by fluctuating river flow renders tidal propagation a non-stationary process, requiring appropriate data analysis methods [Jay and Flinchem, 1997]. Also, quasi-stochastic forcing, due to dam-released high-frequency discharge waves, contaminates the natural tidal frequency spectrum. The general dilemma in analyzing of non-stationary processes is the need to extract instantaneously information about frequencies, while the definition of "frequency" through oscillations with time, implies some time extent. Thus, there is a tradeoff between the length of the time window used to analyze data and the precision with which the filter can retrieve frequency information, as formulated by the Heisenberg uncertainty principle [Landau and Lifshitz, 1976]. Since astronomical tidal frequencies are well known, conventional harmonic analysis of long records is very efficient for stationary tides. A least-squares fit, however, responds inconsistently to non-tidal variance, when the short windows needed here are used [Jay and Flinchem, 1999]. To optimally extract tidal species properties for non-stationary tidal data, we employ wavelet filters [Flinchem and Jay, 2000]. For retrieving tidal range, we use a non-linear filter that determines daily extrema, with the resulting range estimates smoothed over a small number of wave cycles.

4.1 Continuous Wavelet Transform

The continuous wavelet transform y is the convolution of a time series with a scaled wavelet. A wavelet is an oscillating function with zero mean and finite energy and duration [see e.g. Kaiser, 1994]. The scaling depends on the analysis frequency scale s , and is characterized by the time dilatation of $1/s$. Like Jay and Flinchem [1997], we use a Kaiser-windowed complex exponential as our basis wavelet filter. The Kaiser window

is employed because it minimizes energy leakage into side-lobes [Kaiser, 1966]. The wavelet Ψ_L has the following form:

$$\Psi_L(t,s) = N_L(s) I_0 \left(\beta \sqrt{1 - \left(\frac{t}{sL} \right)^2} \right) \exp \left(2\pi i \frac{t}{s} \right) \quad (4.1.1)$$

where I_0 is a zero-order modified Bessel function of the first kind, $\beta = 6.755$ determines the frequency roll-off, and L establishes the wavelet length relative to s , and $N_L(s)$ is chosen such that the maximal response to a unit wave is one. The modified wavelet transform y_L is then defined by:

$$y_L(t,s) = [z * \text{conj}(\Psi_L(s))] (t) \quad (4.1.2)$$

where $*$ is the convolution operator, $\text{conj}(\cdot)$ the complex conjugate of the argument, and z the tidal record. In conventional wavelet transforms, the length of the wavelet filter is proportional to s , so that higher frequencies have a relatively short window with poor frequency resolution. We have increased the window length for frequencies higher than D_2 to improve the frequency resolution, at a small cost in temporal resolution. The filter length is selected, so that a) it corresponds to the time-scale of non-stationary process (e.g. changes in river discharge) and b) the filter responds primarily to particular tidal species. If the filter is too long (yielding good frequency resolution, but poor time resolution) the response is to selective constituents at discrete frequencies. If a filter is too short filter (good time resolution, but poor frequency resolution) it samples multiple tidal species. Filter lengths of 96h and 168h were used for D_1 and D_2 respectively. For scales smaller than D_2 , the window is $20 s$ long; for scales greater than D_1 the window measures $5.6 s$. These choices provide time resolution consonant with the time variability of the river flow, and sufficient frequency resolution to separate tidal species.

4.2 Tidal Range Filter

Before analyzing the tidal range, the sub-tidal river stage needs to be removed, using a high pass filter, since it does not contribute to the actual tidal range. This is plausible, keeping in mind that the daily tidal range can be smaller than the daily sub-tidal variation (due to changes in river discharge) at upriver locations. If low-frequency components are not removed, a range filter could measure the sub-tidal variation rather than the variation due to ocean tides.

$$y(t) = [z * filter_{HP}](t) \quad (4.2.1a)$$

where $filter_{HP}$ is a three-day high pass filter. Non-linear maximum and minimum filters can then be constructed to determine tidal range by:

$$y_{\max}(t) = \max_i(bw(t_i - t)y(t_i)) \quad (4.2.1b)$$

$$y_{\min}(t) = \min_i(bw(t_i - t)y(t_i)) \quad (4.2.1c)$$

where $y(t_i)$ is the variable y sampled at point t_i , and $bw(t)$ a 27h square window with unit amplitude, centered at $t = 0$. The smoothed tidal range z_R is thus retrieved by the operation

$$z_R(t) = [(y_{\max} - y_{\min}) * filter_{LP}](t) \quad (4.2.1d)$$

where $filter_{LP}$ represents a four-day low pass filter. The final smoothing is advantageous, averaging out more irregular contributions due to meteorological effects and instrumental noise. This averaging also produces a signal smoothed over the same time scales as the D_2 tide. Hourly sampling does not capture the extrema to produce an ideal estimate of range, so that we have used more frequently sampled data where available. Nonetheless, results of the tidal range analyses are weakly dependent on the sampling interval Δt .

4.3 Data

Hourly (or more frequent) tide gauge data, recorded between 1980 and 2000, were available from 20 stations along the LCR (Fig. 2.3, Table 1) from the National Ocean Service (NOS), the US Geological Survey, and the National Weather Service. The record length for each station varied between several months (e.g. Knappa) to >20 years (Astoria). We chose Fort Stevens at rkm-13 as reference station for a number of reasons: a) tides at this location are only weakly influenced by river flow (i.e. nearly stationary), b) the station is close to the main channel and as such records the dominant tide propagating into the river, and c) the record was long enough to confidently retrieve harmonic constants. Fort Stevens tidal data were, unfortunately, not available for the entire 1980-2001 period. Incoming ocean tides were, therefore, predicted for all times with harmonic constants from Fort Stevens, derived by a harmonic analysis.

Daily flow values for Beaver (rkm-87) before 1991 were estimated by the weighted sum of flows from the CR (measured at Bonneville Dam, rkm-234) plus the flow of the Willamette River, which enters the LCR at rkm-165. The Willamette River discharge is multiplied by a factor of 1.65 to include the additional contributions of flow from other Coastal Subbasin tributaries, most of which are not consistently gauged [Jay, 1984]. Differences in timing of flows from Coastal Subbasin tributaries are generally small relative to the four to six day averaging in the filters, but some inaccuracies in amplitudes of winter freshets are inevitable. Since 1991, daily flows have been measured at Beaver (rkm-87) by the US Geological Survey. Flow at Beaver is a reasonable flow estimate for the analysis for all gauging stations, because the tidal wave interacts to lowest order with river flow at Beaver. For example, tides measured at Washougal (rkm-190) interact for ~165km with Willamette River flow in addition to the CR flow measured at Bonneville Dam, and only for the last 25km landward the Willamette River flow is excluded. There are several reasons why the daily river flow values remain uncertain: 1) the presence (1981-91) of ungauged tributaries between Bonneville and Beaver that usually contribute 3%, but in exceptional circumstances, 10-15% of the total flow at Beaver, 2) unmeasured flow below Beaver of ~1-10% of Beaver flow, and 3) random errors in measured daily flow as high as 5%, especially at Beaver, where stage is

tidally influenced. Random errors and uncertainties due to tributary inflows are, however, reduced by smoothing river discharge over the time scales of the wavelet filters.

5 Results and Discussion

Results presented here emphasize the predictions of D_1 and D_2 amplitudes, and tidal range. Nonetheless, any complete tidal method must provide predictions for D_1 and D_2 phases as well as overtide characteristics. Our approach did this quite successfully, also, as demonstrated below.

5.1 Modulation of the Oceanic Tidal Frequency Spectrum

Frictional dissipation causes estuarine tidal propagation to be a nonlinear phenomenon, steepening and distorting the tidal wave (Fig. 5.1, panel 2 and 3) [Parker, 1991]. Panel 1 in Fig. 5.1 shows a tidal height record at Astoria (rkm-29), a station close to the mouth and therefore most influenced by ocean tides. The sequence of panels shows tidal height records of stations with increasing upriver distance during a period in 1981 when most data records are available. The last panel in Fig. 5.1 shows the least tidally influenced surface elevation record at Bonneville Dam at rkm-234, where water surface elevation is strongly affected by power peaking and river flow. The intermediate stations in Fig. 5.1 demonstrate intermediate properties between these extremes. The generation of overtides and fluvial damping control evolution of the tidal frequency spectrum, up to about Columbia City (rkm-135). The ocean tidal wave was accordingly modulated with upriver distance and river flow (Fig. 5.1 and 5.2). The dominant overtide species was D_4 , generated from D_2 by frictional interaction. The strength of D_4 relative to the sixth-diurnal at Columbia City suggests that quadratic interactions (related to p_2 and river flow) were more significant than cubic interactions. This is consistent with the behavior of p_2 and p_3 in (3.3.5) for high discharge rates. The more complex modulation of the smaller D_1 component [Godin, 1999] is less apparent in Fig. 5.2 because D_1 is relatively weak. With increasing distance landward, tidal amplitude reduction and wave steepening result

from dissipation and the generation of overtides respectively. Landward of Columbia City (rkm-135), the form and evolution of the tidal spectrum change, suggesting additional physical processes are at work. In this region, a lesser degree of wave steepening and an increase in D_1 amplitudes suggest the superposition of seaward-propagating downriver discharge waves from Bonneville Dam (Fig. 5.1, panel 2 to 4). Interference of tidal and discharge waves is, for example, evident on day 68 as far downriver as at Columbia City (Fig. 5.2, panel 2 and 3). Generally, the tide changed its character from nearly stationary and band-limited at Astoria (where horizontal lines in Fig. 5.2 indicate wave processes) to non-stationary and broadband in the reach above Portland (rkm-170), where vertical "event cones" dominate the scaleogram.

Irregular power peaking cycles at Bonneville Dam generate the event-like fluctuations in Fig. 5.2; they are often larger than the tides for approximately 60 km downriver from the dam. At Bonneville, energy was present in the band from about 1/16 to 2 cycles per day; probably only the D_2 component is primarily tidal. Stochastic high-frequency discharge waves (frequencies greater than 2 d^{-1}) were rapidly damped out downriver from Washougal (rkm-190). Irregular waves with periods of 1 to 4 days traveled downstream and still had an excursion on the order of 0.05 m at Columbia City (Fig. 5.2). Of all the dam-related fluctuations, the weekly power-peaking cycle, with an amplitude of 0.1 m, appears to be the most regular, but this is partially due to the smoothing effect of the filter required to detect energy in this band.

In summary, the spatial analysis of LCR water level frequency spectra suggests that the influence of discharge waves was weak seaward of Columbia City at rkm-135 and that tidal energy input and fluvial dissipation dominate the frequency spectrum from the estuary entrance to Vancouver, rkm-171. Consistent with this qualitative assessment, tidal coefficients π_i , $i=0,1,2$, from the estuary entrance up to Vancouver (rkm-171) displayed relatively little variability, compared to the variability of the coefficients calculated landward of Vancouver.

5.2 Model coefficients

We determined the three amplitude coefficients π_0 , π_1 , and π_2 from (3.4.4a) as function of x for the D_1 and D_2 amplitudes and tidal range. With knowledge of these coefficients we are able to predict the dominant tidal amplitudes and range. The spatial variability of these coefficients also provides important information about tidal processes.

5.2.1 River Flow Coefficient π_1

Data analyses confirm the approximately linear relationship (3.4.4a) between river flow and log-normalized tidal amplitudes (Fig. 5.3); (3.4.2) implies further that the damping modulus should be linearly dependent on discharge. Tidal damping also grows with upriver distance, since the damping exponent xr increases with x . If the Tschebyshev coefficients were independent of Q_R , (3.4.3a) would provide a linear relationship between the π_1 and upriver location.

The Tschebyshev coefficients p_i depend, however, on the ratio of tidal to river flow (Fig. 3.2), and thus vary along the river and with changing discharge. Still, they are, to first order, constant where either tidal or river flow currents are dominant, and p_2 is mainly responsible for tidal damping through river flow. Close to the estuary, the influence of coefficient p_2 is small, so that π_1 decreases only slowly for the first 50-rkm (Figs. 3.2 and 5.4). With increasing upriver distance, the tidal influence weakens and p_2 steadily increases, causing π_1 to become more negative (Fig. 5.4). At the point where the current does not reverse anymore (roughly landward of Beaver, rkm-87, for average flow conditions), p_2 reaches a maximum and is constant thereafter. The interannual variation in the π_1 coefficient at Beaver is likely explained by the fact that currents reverse only during low flow seasons, and current reversal is more frequent in low-flow years (see also Appendix C). From Beaver landward, the slope of π_1 with x is maximal and nearly constant, as expected from the form of p_2 in Fig. 3.2.

The drag coefficient c_D can be estimated from (3.4.3a) and with the definition of $c_1'(x)$ in Appendix A. The average calculated c_D for semidiurnal amplitudes was $5.4 \cdot 10^{-3}$, with a standard deviation of $1.5 \cdot 10^{-3}$. For our determination of c_D , we used all available 10 station-years of data in the reach from rkm-100 to 175 where currents don't reverse, but tidal amplitudes are still large enough for tidal analysis. Non-reversing currents allow the estimation of the bracketed term that involves the Tschebyschev coefficients (see c_1' in Appendix A). The channel width was assumed to linearly converge from 1250m at rkm-100 to 800m at rkm-175, and channel depth and U_s were set equal to 10m and 1ms^{-1} , respectively. Our estimated drag coefficient is a somewhat larger than the value determined by *Giese and Jay* [1989], $c_D = 3 \cdot 10^{-3}$. The latter estimate was made, however, based on model performance in a more seaward reach from rkm-20 to 135. Our value is greater, either because bedforms are larger farther upriver (increasing bed roughness), or because the *Giese and Jay* model did not include topographic convergence in the wave number, altering both wave propagation and damping.

For the river flow coefficient π_1 , the regression analysis provided similar results for D_1 and D_2 amplitude and tidal range (Fig. 5.4). The coefficient for tidal range π_{1R} is between π_{1D2} and π_{1D1} , as (3.5.3) suggests. Thus, tidal range reflects the influence of both species. According to (3.4.2), the ratio of D_2 to D_1 damping modulus should be approximately $\sqrt{2}$. The ratio, however, is close to unity, perhaps because the complex interactions that damp the smaller D_1 species are not fully reflected in (3.4.2).

The more complex damping of D_1 generally causes greater variability in the calculated values of river flow coefficient π_1 (see Fig.7). There are two further reasons why π_1 behaves more erratically for D_1 than for D_2 and tidal range: 1) diurnal discharge waves from Bonneville Dam contribute to observed D_1 values, and 2) the longer D_1 filter cannot resolve the more rapid flow fluctuations. River flow can change significantly over a period of 7 days, roughly the length of the D_1 filter. The shorter windows of the tidal range and D_2 filters provide results more closely matched to the actual scales of flow variability.

The behavior of π_1 with upriver distance further suggests the division of the system into four regimes. In the first reach seaward of rkm-50, the slope of $\pi_1(x)$ is nearly constant. The slope changes in the second reach (between rkm-50 and rkm-90) to a

second nearly constant value. This value is smaller (more negative, corresponding to a larger value of c_D) than the value from the first regime, and defines the third regime roughly from rkm-90 to rkm-175. Further upriver, in the fourth regime, calculated π_1 is erratic, indicating that tidal influence is weaker than power-peaking from Bonneville Dam. This four-fold division modifies the three-regime description of the channel defined by Jay *et al.* [1990]. Our first regime includes the tidally dominated and dissipation-minimum region, while the transition zone begins at the landward end of the dissipation-minimum region. The fluvial energy region as defined by Jay *et al.* [1990] is here divided into ocean-tidal and dam-wave influence regimes.

5.2.2 Neap-Spring Coefficient π_2

The neap-spring variation of the normalized tidal amplitude is due to the quadratic bed stress term and causes a larger rate of along-channel decrease in amplitude for larger incoming tidal amplitudes [Jay *et al.* 1990, Godin, 1990]. Although the tidal amplitude in the π_2 term of the regression model (3.4.4a) should in principle be modeled by half the tidal range $R(0)/2$ for D_2 , D_1 , and R , the best results for D_2 were achieved by modeling incoming ocean tides with the semidiurnal ocean amplitude $D_2(0)$ instead of $R(0)/2$. This is plausible, considering the dominant character of the semidiurnal wave. The coefficient π_2 decreased up to roughly Beaver (rkm-87) and thereafter varied about a constant value, with a relative standard deviation of $\sim 30\%$ (Fig. 5.5).

The Tschebyshev coefficients that represent tidal self-damping are p_2 and p_3 , but only p_3 represents non-linear damping (3.3.5) that influences neap-spring variability and affects the complex wave number. The linear behavior of p_1 is "hidden" in the normalization of tidal amplitudes by the incoming ocean tides. Thus, aside from nonlinearities and changes in p_1 related to Q_R , an increase in entrance amplitude causes a linear increase throughout the system. Our discussion focuses, therefore, on p_3 . Both p_1 and p_3 decrease, as river flow becomes dominant; they vanish at the point where the current no longer reverses (Fig. 3.2). Even though p_3 approaches zero upriver, tidal energy has been both dissipated and transferred to overtides. Since at any location x ,

damping is the sum of damping from the ocean to x , it is more physically accurate to interpret the effect of p_3 using its alongchannel average P_3 , given by:

$$P_3(x) = \frac{1}{x} \int_0^x p_3(x') dx'.$$

This is also applicable for p_2 , but the spatial progression of p_2 is such that $p_2 x$ resembles $\int_0^x p_2(x') dx'$. The normalized integral P_3 is shown as a function of x in Fig. 3.2, assuming that currents reverse seaward of rkm-87 (Beaver). The spatial dependence of P_3 closely resembles that of the observed π_2 (Figs. 3.2 and 5.5).

The neap-spring coefficient was not significantly different for D_1 , D_2 , and R , especially in light of its relatively large degree of random variability at upriver stations (Fig. 5.5), which is consistent with (3.4.2) and (3.5.3). The greater uncertainty of π_2 , compared to π_1 , reflects the simplicity of the neap-spring model. At more seaward stations, neap-spring variations were well-captured for D_2 and R . Deviations occur for high flows, which could be due to uncertainties in discharge. The model is robust against uncertainties in great river discharge because tidal range is weaker further upriver and for larger discharge. Thus, tidal range is small and the absolute errors remain small.

5.2.3 Geometry Coefficient π_0

The coefficient π_0 represents geometry properties in (3.4.3c) through $\log(A(0)/A(x))$, which describes the topographic funneling. Because friction dominates wave propagation, amplitude variations related to topographic funneling do not obey Green's Law [Jay, 1991]. For exponentially convergent geometry, π_0 increases linearly with increasing x . For constant cross-section, roughly the situation landward of rkm-60 [Giese and Jay, 1989], π_0 should converge to a constant value. The results for π_0 suggest spatial variability that cannot be clearly resolved (Fig. 5.6). Changes in π_0 are due to irregular channel geometry, the presence of intertidal areas seaward of \sim rkm-60 (not considered in our model), the dependence of cross-section on river stage, uncertainties in river flow values, and perhaps also the simplifications involved in (3.4.2)-(3.4.4). Since the cross-sectional area decreases by no more than a factor of 2 landward of rkm-50, π_0

should be positive and small. Taking $\pi_0 = 0.15 \approx 1/2 \log(4/3)$ for reconstruction of tidal amplitudes is consistent with our analysis results. Since this value is close to zero and enters exponentially into the model, uncertainties in π_0 do not significantly affect model accuracy.

5.3 Reconstruction of D_2 , D_1 , and R Amplitudes

The modeled and observed tidal amplitudes are generally in agreement for stations from Jetty A (rkm-5) to Vancouver (rkm-171) (Table 2, Fig. 5.7). For the year and station specific coefficients, the rms (root mean square error, see Appendix C) averaged over all station-years relative error is <3.5% for D_2 and tidal range R , and 9% for D_1 , (see also Table 4a). If tidal amplitudes are reconstructed using the coefficients taken from the fitted curves (Figs. 5.4, 5.5, and 5.6), hereafter referred to as the "universal coefficients", the average error increased to 9%, 8%, and 17% for D_2 , R , and D_1 respectively (see also Table 4b). Perhaps more important for prediction purposes than the relative errors, which grow during high flow periods, when tides are small, are the absolute errors. The rms absolute errors for the specific coefficients are all between 25 and 30 mm, but decrease during high flow periods, as tidal amplitudes decrease. As with the relative errors, use of the universal coefficients slightly more than doubles the errors. Although use of the universal coefficients causes somewhat larger errors in hindcasts, the curves from which they are defined allow prediction for any combination of flow and tidal input at any point seaward of Vancouver. For a more detailed error analysis, refer to Appendix C.

These relatively small error ranges validate the usage of the model for hindcasting historic conditions employing the universal coefficients. The relatively large D_1 error, as discussed in the previous section, is not a major issue for predicting R , because D_1 is a smaller contribution to the tidal range than D_2 ; errors for R are comparable to those for D_2 . Neap-spring variations are well resolved for D_2 and R . Uncertainties in river discharge and variations in channel cross-section convergence with flow do not appear to significantly affect the model accuracy. This is because the CR geometry convergence rate is generally close to zero (no strong topographic funneling) and tidal range is only a weak function of river discharge at the high flow levels. One reason why flow-related

variations in cross-sectional area with flow are of little importance in the 1980-2000 data is the presence of flood control dikes. These dikes prevent significant overbank flow for flows $<24,000 \text{ m}^3\text{s}^{-1}$, stabilizing the width of the river. Flows exceeded this level only twice during the 1980-2000 period, for a total of less than a week.

It is also useful to compare the results achieved here with those of previous studies. Our approach of objectively fitting coefficients for each tidal species provides better results than obtained from the semi-analytical model of *Giese and Jay* [1989], which is similar to *Jay* [1991]. In this model c_D was the only parameter, and it varied systematically with Q_R . That model's M_2 amplitude prediction error was 5% for stations seaward of rkm-90, and greater errors were found for tidal height predictions further landward. The largest improvement is made for D_2 amplitudes far upriver and during periods with high river discharge. Thus, model results can be improved through an objective, data-driven approach to the representation of frictional energy. This confirms that the form of the bed stress representation (including effects of river discharge and neap-spring variability) is crucial to achieving accurate predictions.

The other potential approach, use of conventional harmonic analysis, is elaborate and requires many tidal constituents. To predict a single tidal constituent, two coefficients are needed, so that six to 30 coefficients are required for the prediction of a particular tidal species. Yet, the addition of constituents corresponding to numerous, small non-linear interactions does not yield improved prediction power for non-stationary flows [*Godin*, 1990], because non-stationary tidal behavior violates the stationarity assumption inherent in modeling tidal species with constituents [*Jay and Flinchem*, 1999]. Fig. 5.8a compares tidal prediction for the semidiurnal tidal amplitude at Columbia City with the new method developed here. The rms is error is 0.062 m for HA vs. 0.025 m for the new method. The HA approach uses 28 coefficients, adjusted to the particular height record for Columbia City in 1981, while the new method uses six coefficients, specific to the tidal height record, and as inputs incoming ocean tides and river discharge. The advantage of the new method over the conventional tidal prediction method is obvious.

The species concordance method [*Simon*, 1990] is reasonably compact and works well for rivers without large or rapid flow variability. However, it is not based on an

analysis of tidal dynamics and model coefficients are chosen by harmonic analysis, so it is limited in its ability to represent a very dynamic system.

Numerical modeling of waves in river channels [Baptista *et al.*, 1999; Salerno and Markman, 1991; Wiele and Smith, 1996] may achieve similar or better accuracy than our prediction method. However, it is also more computationally demanding. As a result, the numerical approach might not be suitable for the tidal predictions over very long time periods, as done for historical reconstructions. Because of the different temporal and spatial prediction capabilities of the numerical and the wavelet-based approaches, they are highly complementary for accurate tidal predictions. Results from our approach provide opportunities for model diagnosis and guidance in the representation of the bedstress in light of its dependency on river discharge and incoming ocean tides.

5.4 Phases

Important tidal information needed to understand historic changes in CR water levels and how these levels affect salmonid habitat are D_1 , D_2 amplitudes and tidal range. Our method can also provide robust hindcasts of phases and overtide properties. The analysis of phases is limited to high quality data records with consistent time control. Unlike elevation errors, timing errors are often not obvious from inspection of a tidal record, but have a major impact on the phase analysis. For example, a timing error of 1h, as frequently occurs during the transition from daylight standard time in the fall, introduces a temporary 60° phase error in D_4 . Such an error is large enough to obscure the dynamical signal we seek.

The 1981 NOS tidal records constitute a data set with both a substantial number of stations and consistent time control. Though the smaller number of station-years limits statistical certainty in determination of the π_i' , the resulting π_{i,D_2}' and π_{i,D_1}' patterns are consistent with our theoretical development (Fig. 5.9). The coefficients π_{1,D_2}' are greater than π_{1,D_1}' , in accord with (3.3.13). As suggested by (3.3.13) and (3.4.2), the magnitudes of the π_i' are close to those of the π_i , for $i=1,2$, but phase and amplitude coefficients have opposite signs. As with the π_i , the phase coefficients π_i' increase in magnitude with upriver distance. The results of reconstructed phases (Fig. 5.10) suggest that D_1 and D_2

phases can, given consistent time control, be modeled with a degree of accuracy similar to that of D_1 and D_2 amplitudes.

5.5 Overtides: D_4

The first overtide (D_4) of the D_2 wave is considered here as representative of the problem of modeling overtides. Using the theoretical development from section 3.6, we are able to predict $|D_4|$ with an average rms error of $<1\text{mm}$, which translates to a relative error of 12% (see also Table 4c). Model results for Altoona, Beaver, Columbia City, and Vancouver are shown in Figs. 5.3b and 5.7b. Because of the non-stationary behavior of river tides, this degree of predictability could not have been achieved with conventional harmonic tidal analysis (Fig. 5.8b).

The results for the phase coefficients for the D_4 wave are summarized in Table 3, showing the ratio of the phase coefficients $\pi_{i,D_4}' / \pi_{i,D_2}'$, where $i=1,2$. Where phase differences are very small (close to the reference station at rkm-13) the ratio is sensitive to the small denominator, and results are erratic. The negative numbers, however, are probably due to the influence of the incoming ocean D_4 wave up to \sim rkm-50. As noted by Jay and Musiak [1996], the D_4 wave undergoes an abrupt 180° phase change at about rkm-35 as the forced wave becomes dominant over the free wave of oceanic origin. After the incident D_4 wave is damped and the fluvial forcing becomes dominant, the ratio $\pi_{i,D_4}' / \pi_{i,D_2}'$ is $O(2)$, as predicted by (3.6.3) (see Table 3). The mean ratio $\pi_{2,D_4}' / \pi_{2,D_2}'$ of the phase neap-spring coefficient landward from rkm-53 is 1.6 with a standard deviation of 1.0. The greater standard deviation of the neap-spring ratio is due to the variability of the neap-spring coefficients, as discussed in section 5.2.2. Both D_4 phase and amplitude have been successfully modeled, suggesting that the method employed herein can be applied to all overtides to complete our new non-stationary tidal model.

6 Summary and Conclusions

We have developed a new method for modeling and hindcasting non-stationary river tides. By applying wavelet tidal analysis methods, an analytical fluvial tide model, and an objective determination of model coefficients to the LCR, we have compactly defined the interactions of tides and river flow in the LCR. The model is based on an analytical solution for incident tidal waves in frictional, convergent channels [Jay, 1991]. We have decomposed the bedstress, such that 1) the effects of variable river flow and incoming ocean tides are represented in a manner consistent with the underlying physics, and 2) the model coefficients can be determined from tidal height data by linear regression analysis. From ~50 station-years of surface elevation records for the LCR we extracted D_1 , D_2 , and D_4 amplitudes and phases by CWT methods [Flinchem and Jay, 2000]. Smoothed tidal range was retrieved by a minimum-maximum filter. The six coefficients per tidal species represent the effects of river flow, neap-spring variability, and geometry. The along-channel distributions of the coefficients can be interpreted in terms of the tidal energy regime of the LCR. In reconstructing tidal amplitudes, the rms model prediction error was <30 mm for R , D_2 , and D_1 amplitude. One of the model's strengths is the rapid, accurate tidal prediction for a very broad range of river discharge. Furthermore, because regression analysis was used to fit the model to the data, the model is relatively robust against inaccuracies in river flow and uncertainties in geometry. Thus, we have modeled non-stationary fluvial tidal properties with a previously unattained level of compactness and accuracy relative to conventional methods. The model can also be used in forecast mode, to the extent that river flow can be predicted.

These results can be used in future work, together with a low-frequency stage model, to hindcast historical water levels in the CR. Relating historical water levels to LCR hypsometric data would allow an assessment of historical changes in the location and properties of salmonid-favorable shallow-water habitat.

References

- Baptista, A. M., M. Wilkin, P. Pearson, P. Turner, C. McCandlish, and P. Barrett, Coastal and estuarine forecast systems. A multi-purpose infrastructure for the Columbia River, *Earth System Monitor*, 9(3), 1-16, 1999.
- Bottom, D. L., C. A. Simenstad, A. M. Baptista, D. A. Jay, J. Burke, K. K. Jones, E. Casillas, and M. H. Schiewe, *Salmon at river's end: The role of the estuary in the decline and recovery of Columbia River Salmon*, US National Marine Fisheries Service, Seattle, 2001.
- Dronkers J. J., *Tidal Computations in Rivers and Coastal Waters*, North-Holland Publishing Company, Amsterdam, 296-304, 1964.
- Flinchem, E. P., and D. A. Jay, An introduction to wavelet transform tidal analysis methods, *Estuarine, Coastal and Shelf Sci.*, 51, 177-200, 2000.
- Friedrichs, C. T., and D. G. Aubrey, Tidal propagation in strongly convergent channels, *J. Geophys. Res.*, 99, 3321-3336, 1994.
- Giese, B. S., and D. A. Jay, Modeling the tidal energetics of the Columbia River Estuary, *Estuarine, Coastal and Shelf Sci.*, 29, 549-571, 1989.
- Godin, G., The tide in the Rivers, *International Hydrographic Review*, Monaco, 61(2), 159-170, 1984.
- Godin, G., Frictional effects in river tides, in *Progress in Tidal Hydrodynamics*, edited by B. B. Parker, 379-402, John Wiley, New York, 1991.
- Godin, G., The propagation of tides up rivers with special considerations on the upper Saint Lawrence River, *Estuarine, Coastal and Shelf Sci.*, 48, 307-324, 1999.
- Green, G., On the motion of waves in a variable canal of small depth and width, *Trans. Cambridge Philos. Soc.*, 6, 457-462, 1837.
- Independent Scientific Group, Return to the river: scientific issues in the restoration of salmonid fishes in the Columbia River, *Fisheries*, 24, 10-19, 1999.
- Jay, D. A., Green's law revisited: Tidal long wave propagation in channels with strong topography, *J. Geophys. Res.*, 96, 20585-20598, 1991.
- Jay, D. A., *Circulatory Processes in the Columbia River Estuary*, Columbia River Estuary Data Development Program, Columbia River Estuary Study Taskforce, Astoria, Oreg., 1984.

- Jay, D. A. *Residual Circulation in shallow stratified estuaries*, Special Report 104, School of Oceanography, University of Washington, Seattle, 1987.
- Jay, D. A., B. S. Giese, and C. R. Sherwood, Energetics and sedimentary processes in the Columbia River Estuary, *Progr. Oceanogr.*, 25, 157-174, 1990.
- Jay, D.A., and J. D. Musiak, Internal tidal asymmetry in channel flows: origins and consequences, in *Mixing in Estuaries and Coastal Seas, Coastal and estuaries Stud.*, edited by C. Pattiaratchi, AGU, Washington, D.C., 50, 211-249, 1996.
- Jay, D. A., and E. P. Flinchem, Interaction of fluctuating river flow with a barotropic tide: A demonstration of wavelet tidal analysis methods, *J. Geophys. Res.*, 102(C3), 5705-5720, 1997.
- Jay, D. A., and E. P. Flinchem, A comparison of methods for analysis of tidal records containing multi-scale non-tidal background energy, *Continental Shelf Res.*, 19, 1695-1732, 1999.
- Kaiser, G., *A friendly guide to wavelets*, Birkhäuser, Boston, 60-72, 1994.
- Kaiser, J. F., Digital filters, in *System analysis by digital computers*, edited by F. F. Kuo and J. F. Kaiser, Jon Wiley, New York, 218- 284, 1966.
- Lamb, H., *Hydrodynamics*, Cambridge University Press, Cambridge, 6th edition, 1932.
- Landau, L. D., and E. M. Lifshitz, *Quantum mechanics*, Pergamon, New York, 46-48, 1977.
- Lanzoni, S., G. Seminara, On tide propagation in convergent estuaries, *J. Geophys. Res.*, 103(C13), 30793-30812, 1998.
- Latif, M., and T. P. Barnett, Causes of decadal climate variability over the North Pacific and North America, *Science*, 266, 634-637, 1994.
- LeBlond, P. H., On tidal propagation in shallow rivers, *J. Geophys. Res.*, 83, 4717-4721, 1978.
- Mantua, N. J., R. C. Francis, S. R. Hare, Y. Zhang, and J. M. Wallace, A Pacific interdecadal climate oscillation with impacts on salmon production, *Bulletin of the American Meteorological Society*, 78(6), 1069-1079, 1997.
- Parker, B. B., The relative importance of the various nonlinear mechanisms in a wide range of tidal interactions, in *Progress in Tidal Hydrodynamics*, edited by B. B. Parker, 237-268, John Wiley, New York, 1991.
- Salerno, J. R., S. Markman, *An evaluation of tidal forecast errors on the Lower Columbia: the Northwest River Forecast Center Dynamic Wave Operational Model*, Hydrologists, National Oceanic and Atmospheric Administration, National Weather Service, Northwest River Forecast Center, Portland, Oregon, 1991.
- Sherwood, C.R., D.A. Jay, R.B. Harvey, P. Hamilton, and C.A. Simenstad, Historical changes in the Columbia River Estuary, *Prog. Oceanog.*, 25, 299-352, 1990.

Sherwood, C. R., J. S. Creager, E. H. Roy, G. Gelfenbaum and T. Dempsy, Sedimentary processes and environments in the Columbia River Estuary, Columbia River Estuary Data Development Program, Columbia River Estuary Study Taskforce, Astoria, Oreg., 1984.

Simon, B., in *Progress in Tidal Hydrodynamics*, edited by B. B. Parker, 725-735, John Wiley, New York, 1991.

Simenstad, C.A., L.F. Small, C.D. McIntire, Consumption processes and food web structure in the Columbia River estuary, *Prog. Oceanog.*, 25, 271-297, 1990.

Thomas, D.W., *Changes in Columbia River habitat types over the past century*, Columbia River Estuary Data Development Program, Columbia River Estuary Study Taskforce, Astoria, Oregon, 1983.

US Coast and Geodetic Survey, *Manual of harmonic constant reductions*, Washington, D.C., 1952.

Wiele, S.M., and J.D. Smith, A reached-averaged model of diurnal discharge wave propagation down the Colorado River through the Grand Canyon, *Water Resources Res.*, 32(5), 1375-1386, 1996.

Tables

Table 1. Station-years available for tidal analysis.

rkm	Station	Years of Record
5	Jetty A	1981
13	Ft Stevens	1981
19	Knappton	1981
29	Astoria	1981-2000
39	Altoona	1981
42	Knappa	1981
54	Skamokawa	1981, 1997-2000
60	Cathlamet	1981
66	Wauna	1981
87	Beaver	1981, 1997-2000
106	Longview	1997-2000
108	Rainier	1981
119	Kalama	1981
135	Columbia City	1981
138	St Helens	1999, 2000
171	Vancouver	1997-2000
190	Washougal	1981
219	Multnomah	1981
228	Warrendale	1981
234	Bonneville Dam	1981, 1992-2000

Table 2. Average rms error for all stations from Jetty A to Vancouver.

Tidal amplitude	Error for specific coefficients		Error for universal coefficients	
	Absolute (mm)	Relative (%)	Absolute (mm)	Relative (%)
D_2	28	3.9	66	8.6
D_1	25	9.2	48	16.5
R	30	3.4	78	7.9

Table 3. Ratio of D_4 phase coefficients to D_2 phase coefficients as function of x .

Upriver distance (rkm)	$\pi_{1,D4}' / \pi_{1,D2}'$	$\pi_{2,D4}' / \pi_{2,D2}'$
5	-12.1	-2.1
13	51.5	1265
19	-98.4	22.6
29	-20.6	6.7
38	13.3	2.2
41	12.9	3.8
53	2.7	2.1
60	2.3	1.1
66	2.1	1.0
87	1.0	0.9
119	2.6	3.4
138	2.2	1.0
Mean +/- standard deviation from rkm-53 to 138	2.2 +/- 0.6	1.6+/-1.0

Table 4a. Amplitude errors for D_2 , D_1 , and R (absolute error in m, relative in %) for the coefficient determined for each station year of tidal data.

year	rkm	D2 (m)	D2(%)	D1(m)	D1(%)	R(m)	R(%)
1981	5	0.022463	0.025432	0.015585	0.035152	0.055017	0.022912
1981	13	0.014185	0.014422	0.010883	0.024739	0.038601	0.014869
1981	19	0.016204	0.016008	0.009668	0.022012	0.042034	0.015886
1981	29.29012	0.022398	0.022395	0.021309	0.051284	0.060546	0.023447
1981	38.6	0.026316	0.027998	0.021816	0.057092	0.063845	0.026184
1981	41.8	0.02018	0.02081	0.01934	0.054247	0.057206	0.022898
1981	53.59126	0.039631	0.045966	0.043032	0.137264	0.059744	0.027273
1981	60.02864	0.027004	0.035546	0.031254	0.097323	0.05746	0.028915
1981	65.98323	0.029143	0.039468	0.031688	0.102804	0.061636	0.031934
1981	86.58287	0.032669	0.053902	0.030989	0.134418	0.077323	0.048652
1981	119.0917	0.015579	0.043795	0.024641	0.155526	0.038971	0.038072
1981	108.47	0.037569	0.08538	0.025024	0.163603	0.081967	0.070313
1981	135.1852	0.024496	0.097871	0.026518	0.234823	0.06955	0.098423
1981	189.903	0.015624	0.35057	0.026544	0.655544	0.07596	0.329691
1981	214	0.005435	0.549943	0.014562	0.644699	0.043517	0.36137
1981	218.8712	0.007883	0.537295	0.031599	0.76858	0.096751	0.499645
1981	234.16	0.025168	0.613715	0.056058	0.753399	0.165769	0.415797
1993	29.29012	0.032796	0.032689	0.031396	0.073169	0.075433	0.02884
1993	86.58287	0.029593	0.048309	0.029236	0.116432	0.062	0.038075
1993	234.16	0.073945	0.769653	0.118093	0.622297	0.280744	0.390327
1994	29.29012	0.01849	0.01826	0.020684	0.050151	0.047747	0.018297
1994	86.58287	0.025078	0.038517	0.033388	0.135947	0.052569	0.030902
1994	234.16	0.056696	0.518874	0.124794	0.675956	0.249869	0.360079
1995	29.29012	0.020791	0.020526	0.025321	0.064739	0.062914	0.024507
1995	86.58287	0.042014	0.069341	0.036029	0.174456	0.107588	0.069367
1995	234.16	0.058744	0.604216	0.149668	0.770324	0.282178	0.389128
1996	29.29012	0.023857	0.023637	0.021504	0.056654	0.054762	0.021582
1996	86.58287	0.038874	0.083112	0.029741	0.180644	0.092344	0.07704
1996	234.16	0.038217	0.687492	0.09607	0.880628	0.18173	0.349359
1997	29.29012	0.026868	0.026557	0.021945	0.057637	0.07089	0.027905
1997	53.59126	0.04714	0.053368	0.028802	0.096145	0.043535	0.02153
1997	86.58287	0.060666	0.095089	0.041516	0.165495	0.067562	0.040037
1997	106.2169	0.029481	0.059815	0.022362	0.157438	0.063666	0.049665
1997	171.3955	0.025015	0.183108	0.030563	0.368305	0.077261	0.178279
1997	234.16	0.047469	0.691767	0.109146	0.734829	0.206667	0.346677
1998	29.29012	0.023118	0.022547	0.017964	0.046025	0.054885	0.021214
1998	53.59126	0.021677	0.022729	0.019833	0.092443	0.022105	0.009712
1998	86.58287	0.029078	0.049311	0.041348	0.166236	0.081153	0.052371
1998	106.2169	0.028404	0.068023	0.011518	0.084418	0.071403	0.067893
1998	171.3955	0.026145	0.100734	0.039602	0.315841	0.088829	0.11725
1998	234.16	0.04072	0.51994	0.089274	0.737686	0.230848	0.418533

Table 4b. Amplitude errors for D_2 , D_1 , and R (absolute error in m, relative in %) for the coefficient determined from the universal coefficients (fitting curves in Figs. 5.4-5.6). A NaN is printed for $rkm > 175km$, because universal coefficients in that reach could not be determined (see text).

year	rkm	D2 (m)	D2(%)	D1(m)	D1(%)	R(m)	R(%)
1981	5	0.370832	0.419858	0.147315	0.332277	0.867317	0.361198
1981	13	0.134133	0.136376	0.078942	0.179446	0.318951	0.122861
1981	19	0.048335	0.047751	0.062334	0.141915	0.121362	0.045866
1981	29.29012	0.034812	0.034807	0.028545	0.068699	0.088415	0.034239
1981	38.6	0.049067	0.052203	0.03337	0.087329	0.120877	0.049574
1981	41.8	0.075973	0.078347	0.0295	0.082743	0.226187	0.090535
1981	53.59126	0.052112	0.060442	0.04926	0.157131	0.117564	0.053667
1981	60.02864	0.037316	0.04912	0.052503	0.163491	0.092618	0.046608
1981	65.98323	0.055272	0.074855	0.043881	0.142363	0.14525	0.075255
1981	86.58287	0.035023	0.057786	0.055817	0.242108	0.094188	0.059263
1981	119.0917	0.114065	0.320664	0.053279	0.336285	0.22819	0.222924
1981	108.47	0.04014	0.091222	0.057323	0.374773	0.093219	0.079965
1981	135.1852	0.057729	0.230647	0.043198	0.382532	0.17485	0.247438
1981	189.903	NaN	NaN	NaN	NaN	NaN	NaN
1981	214	NaN	NaN	NaN	NaN	NaN	NaN
1981	218.8712	NaN	NaN	NaN	NaN	NaN	NaN
1981	234.16	NaN	NaN	NaN	NaN	NaN	NaN
1993	29.29012	0.045084	0.044937	0.036949	0.086109	0.105993	0.040524
1993	86.58287	0.054631	0.089181	0.040552	0.161496	0.15011	0.092184
1993	234.16	NaN	NaN	NaN	NaN	NaN	NaN
1994	29.29012	0.033919	0.033497	0.027564	0.066832	0.083351	0.03194
1994	86.58287	0.026886	0.041295	0.048466	0.197344	0.086355	0.050764
1994	234.16	NaN	NaN	NaN	NaN	NaN	NaN
1995	29.29012	0.040958	0.040437	0.034472	0.088139	0.090312	0.035179
1995	86.58287	0.059646	0.098443	0.039895	0.193174	0.162794	0.10496
1995	234.16	NaN	NaN	NaN	NaN	NaN	NaN
1996	29.29012	0.055174	0.054667	0.031607	0.083269	0.102318	0.040324
1996	86.58287	0.064926	0.138811	0.03554	0.215865	0.154852	0.129188
1996	234.16	NaN	NaN	NaN	NaN	NaN	NaN
1997	29.29012	0.056568	0.055914	0.029458	0.07737	0.112397	0.044243
1997	53.59126	0.065019	0.073608	0.052934	0.176701	0.085065	0.04207
1997	86.58287	0.039291	0.061585	0.055532	0.221366	0.133839	0.079313
1997	106.2169	0.034716	0.070435	0.060162	0.423565	0.069603	0.054296
1997	171.3955	0.041829	0.306187	0.039412	0.474931	0.096721	0.223183
1997	234.16	NaN	NaN	NaN	NaN	NaN	NaN
1998	29.29012	0.051031	0.049769	0.025661	0.065744	0.103695	0.04008
1998	53.59126	0.052429	0.054974	0.024252	0.113041	0.072053	0.031658
1998	86.58287	0.042381	0.071869	0.056132	0.225673	0.148426	0.095785
1998	106.2169	0.028659	0.068634	0.036106	0.264639	0.076777	0.073002
1998	171.3955	0.044247	0.170476	0.043982	0.350776	0.101322	0.13374
1998	234.16	NaN	NaN	NaN	NaN	NaN	NaN

Table 4c. D_4 Amplitude errors (absolute error in m, relative in %) for 1981. See also section 5.5.

rkm	D4(m)	D4(%)
5	0.006954	0.237969
13	0.005641	0.18308
19	0.006842	0.297599
29.29012	0.00676	0.406454
38.6	0.00608	0.132746
41.8	0.005089	0.080557
53.59126	0.004836	0.059397
60.02864	0.004627	0.051935
65.98323	0.00553	0.060627
86.58287	0.008459	0.078945
108.47	0.008909	0.091689
119.0917	0.007877	0.078786
135.1852	0.005728	0.096199
189.903	0.003126	0.358249
228	0.001366	0.49299
218.8712	0.003399	0.792113
234.16	0.007381	0.531623

Table 5a. For each station year of tidal data determined coefficients π_0 , π_1 , and π_2 for semidiurnal tidal amplitude.

year	rkm	π_0	π_1	π_2
1981	5	-0.20844	0.007656	0.106937
1981	13	0.004109	-0.00073	0.000378
1981	19	0.141844	-0.00803	-0.12282
1981	29.29012	0.151886	-0.01007	-0.15987
1981	38.6	0.161647	-0.01498	-0.23387
1981	41.8	0.169739	-0.01666	-0.19403
1981	53.59126	0.207191	-0.03166	-0.35227
1981	60.02864	0.219076	-0.04031	-0.40638
1981	65.98323	0.23984	-0.04606	-0.41499
1981	86.58287	0.146803	-0.07376	-0.36527
1981	119.0917	-0.24478	-0.11307	-0.43936
1981	108.47	0.253053	-0.14756	-0.31698
1981	135.1852	-0.06452	-0.18734	-0.34192
1981	189.903	-1.25761	-0.30522	-0.16762
1981	214	-1.49481	-0.28478	-0.47044
1981	218.8712	-1.88631	-0.22619	-1.12506
1981	234.16	-1.50136	-0.20624	-0.99655
1992	29.29012	0.220093	-0.02066	-0.17654
1992	86.58287	-0.06602	-0.02625	-0.4886
1992	234.16	-1.41899	-0.16191	-0.39446
1993	29.29012	0.166163	-0.01108	-0.1607
1993	86.58287	0.021493	-0.05293	-0.29629
1993	234.16	-1.40612	-0.18577	-0.04234
1994	29.29012	0.201813	-0.02024	-0.15131
1994	86.58287	-0.07318	-0.03851	-0.31025
1994	234.16	-1.43627	-0.182	-0.11775
1995	29.29012	0.207621	-0.01475	-0.19284
1995	86.58287	0.056422	-0.06299	-0.26678
1995	234.16	-1.28832	-0.13648	-0.72427
1996	29.29012	0.208327	-0.0129	-0.19859
1996	86.58287	0.130709	-0.06899	-0.3212
1996	234.16	-1.43278	-0.12446	-1.10466
1997	29.29012	0.207039	-0.01163	-0.22296
1997	53.59126	0.275642	-0.04059	-0.42269

year	rkm	π_0	π_1	π_2
1997	86.58287	0.311113	-0.08947	-0.61418
1997	106.2169	0.189448	-0.1262	-0.37636
1997	171.3955	0.487353	-0.3314	-0.17245
1997	234.16	-1.34134	-0.15835	-0.5348
1998	29.29012	0.169891	-0.00993	-0.16144
1998	53.59126	0.084414	-0.02518	-0.19015
1998	86.58287	0.031719	-0.05711	-0.29284
1998	106.2169	-0.09562	-0.08554	-0.4028
1998	171.3955	0.152332	-0.26995	-0.29963
1998	234.16	-2.1481	-0.06288	-0.26305
1999	29.29012	0.209125	-0.01263	-0.21017
1999	86.58287	0.196321	-0.07605	-0.33683
1999	106.2169	0.140118	-0.1162	-0.35449
1999	138.4038	0.053197	-0.20927	-0.15449
1999	171.3955	0.311254	-0.30407	-0.14919
1999	234.16	-1.9393	-0.10297	-0.25484

Table 5b. For each station year of tidal data determined coefficients π_0 , π_1 , and π_2 for diurnal tidal amplitude.

year	rkm	π_0	π_1	π_2
1981	5	-0.09102	0.003107	0.109575
1981	13	0.018146	-0.00164	-0.00621
1981	19	0.106249	-0.00935	-0.07887
1981	29.29012	0.097788	-0.00759	-0.12407
1981	38.6	0.078096	-0.01495	-0.16296
1981	41.8	-0.08021	0.000468	-0.06066
1981	53.59126	0.028815	-0.02098	-0.19547
1981	60.02864	0.149399	-0.03429	-0.40065
1981	65.98323	0.166164	-0.03797	-0.41878
1981	86.58287	-0.06674	-0.05091	-0.32644
1981	119.0917	0.043571	-0.09491	-0.66038
1981	108.47	-0.58917	-0.01478	-0.41187
1981	135.1852	0.034286	-0.18385	-0.2851
1981	189.903	-0.9698	-0.19603	-0.27097
1981	214	-0.69841	-0.23312	0.073638
1981	218.8712	-0.17603	-0.24448	-0.50339
1981	234.16	-0.64105	-0.14359	-0.40601
1992	29.29012	0.024034	0.003708	-0.0836
1992	86.58287	-0.35935	0.010243	-0.35937
1992	234.16	0.67536	-0.19644	-0.87074
1993	29.29012	0.095232	-0.00852	-0.1135
1993	86.58287	0.054816	-0.05419	-0.38999
1993	234.16	1.223967	-0.25158	-1.03995
1994	29.29012	0.116549	-0.0048	-0.15163
1994	86.58287	-0.43856	0.012447	-0.29329
1994	234.16	0.219728	-0.04937	-1.13616
1995	29.29012	0.099911	-0.00522	-0.16497
1995	86.58287	-0.2821	-0.02791	-0.27841
1995	234.16	1.578554	-0.2556	-1.14895
1996	29.29012	0.103954	-0.00629	-0.17917
1996	86.58287	-0.14149	-0.04226	-0.36892
1996	234.16	1.085041	-0.20705	-0.98452
1997	29.29012	0.147643	-0.01141	-0.15385
1997	53.59126	0.019518	-0.03887	-0.31145

year	rkm	π_0	π_1	π_2
1997	86.58287	0.333993	-0.10014	-0.56489
1997	106.2169	0.055051	-0.11282	-0.36674
1997	171.3955	0.808574	-0.26976	-0.45615
1997	234.16	1.515766	-0.24202	-0.93113
1998	29.29012	0.0978	-0.00813	-0.11635
1998	53.59126	-0.05086	-0.03377	-0.16877
1998	86.58287	0.015076	-0.05579	-0.36046
1998	106.2169	-0.19896	-0.06433	-0.48671
1998	171.3955	-0.31815	-0.16683	-0.05032
1998	234.16	-0.85584	-0.0327	-0.24885
1999	29.29012	0.11311	-0.00759	-0.15758
1999	86.58287	-0.02363	-0.05767	-0.34581
1999	106.2169	0.189896	-0.11409	-0.36263
1999	138.4038	0.263581	-0.20046	-0.11985
1999	171.3955	0.467632	-0.25295	-0.09317
1999	234.16	1.177834	-0.22064	-0.91919

Table 5c. For each station year of tidal data determined coefficients π_0 , π_1 , and π_2 for tidal range.

year	rkm	π_0	π_1	π_2
1981	0	-0.17928	0.00624	0.091067
1981	13	0.018529	-0.00185	-0.00022
1981	19	0.127844	-0.00795	-0.06273
1981	29.29012	0.149861	-0.01005	-0.10916
1981	38.6	0.174392	-0.01649	-0.16296
1981	41.8	0.158519	-0.01488	-0.11793
1981	53.59126	0.203309	-0.02764	-0.25336
1981	60.02864	0.206324	-0.03819	-0.26254
1981	65.98323	0.229084	-0.04383	-0.27199
1981	86.58287	0.147207	-0.06945	-0.25397
1981	119.0917	-0.16695	-0.0919	-0.36799
1981	108.47	0.079666	-0.11403	-0.20116
1981	135.1852	0.03252	-0.18514	-0.24257
1981	189.903	-0.85736	-0.16999	-0.71619
1981	214	-0.8328	-0.15987	-0.84649
1981	218.8712	0.075594	-0.22819	-1.08102
1981	234.16	-0.52998	-0.12728	-0.79873
1993	29.29012	0.179212	-0.01267	-0.11798
1993	86.58287	0.125177	-0.05735	-0.27134
1993	234.16	0.072519	-0.14028	-0.73496
1994	29.29012	0.194256	-0.01806	-0.10937
1994	86.58287	0.024556	-0.04285	-0.27319
1994	234.16	-0.52778	-0.05386	-0.68911
1995	29.29012	0.186786	-0.01325	-0.12875
1995	86.58287	0.135462	-0.06512	-0.24114
1995	234.16	0.119269	-0.11633	-0.95466
1996	29.29012	0.210462	-0.01297	-0.15779
1996	86.58287	0.143274	-0.06515	-0.26248
1996	234.16	0.026029	-0.10969	-1.00257
1997	29.29012	0.212973	-0.01271	-0.16436

year	rkm	π_0	π_1	π_2
1997	53.59126	0.253869	-0.0324	-0.32895
1997	86.58287	0.142969	-0.07381	-0.17701
1997	106.2169	0.228978	-0.12327	-0.27831
1997	171.3955	0.492559	-0.25918	-0.49137
1997	234.16	0.304091	-0.13887	-0.98616
1998	29.29012	0.18554	-0.01164	-0.12973
1998	53.59126	0.157485	-0.03065	-0.19451
1998	86.58287	0.059178	-0.06239	-0.14599
1998	106.2169	0.117857	-0.09689	-0.35954
1998	171.3955	-0.02366	-0.21281	-0.18552
1998	234.16	-1.03556	-0.00095	-0.66366
1999	29.29012	0.221577	-0.01376	-0.16283
1999	53.59126	0.19976	-0.02957	-0.24048
1999	86.58287	0.245683	-0.07572	-0.26117
1999	106.2169	0.287211	-0.12393	-0.26303
1999	138.4038	0.160424	-0.20267	-0.14806
1999	171.3955	0.263656	-0.25254	-0.19345
1999	234.16	-0.07954	-0.11996	-0.65403

Figures

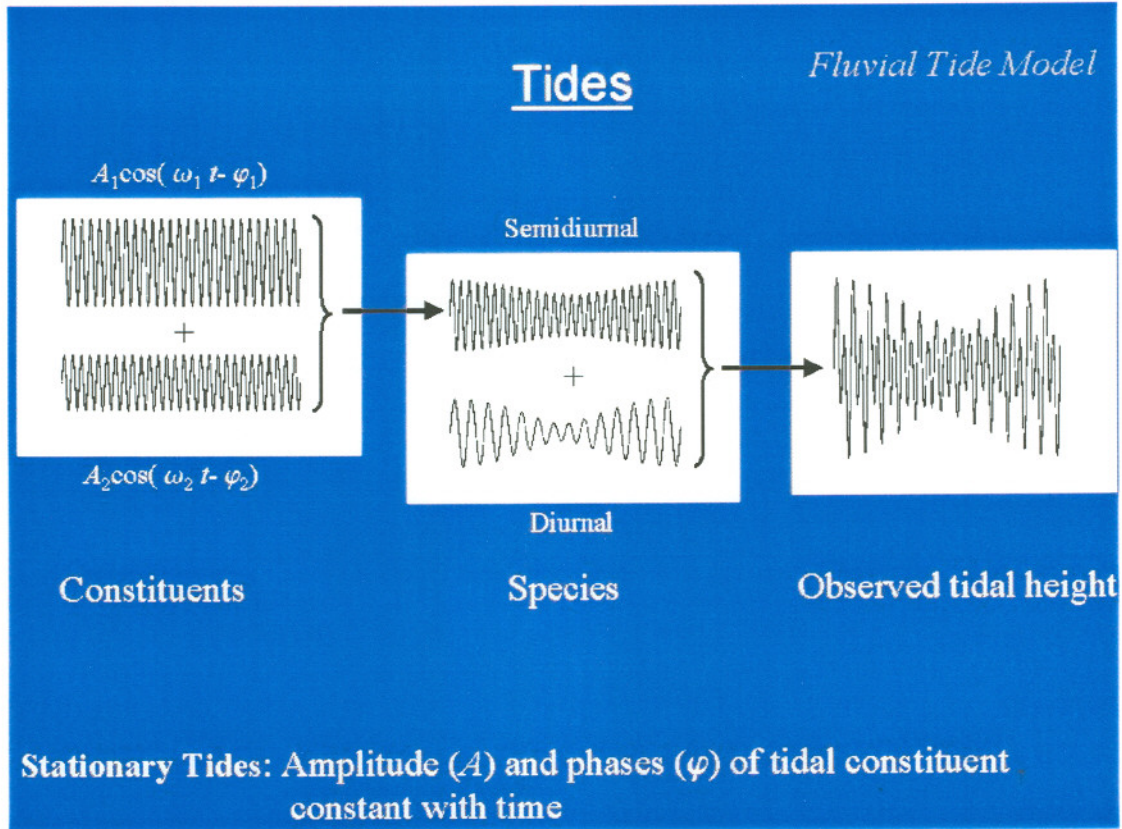


Fig. 1.1. Concept of tidal constituents and species in the context of stationarity. Two semidiurnal tidal constituents with frequencies ω_1 and ω_2 , amplitudes A_1 and A_2 , and phases φ_1 and φ_2 are shown in the left panel. All semidiurnal constituents add up to form a semidiurnal species. The middle panel shows a semidiurnal and diurnal tidal species. All tidal species together make up the observed tidal height, here schematically shown in the right panel with only two tidal species (consisting of two tidal constituents each). Tides are stationary if the phase and amplitude of each tidal constituent are constant with time. We refer to "spring tides" if tidal constituents of one species interfere constructively, so that their amplitudes add up. If tidal constituent of one species interfere destructively, resulting in smaller tidal amplitudes, we call this "neap tide".



Fig. 2.1. Watershed of the Columbia River (light gray); black dots represent major dams. Figure adapted from the US Army Corps of Engineers.

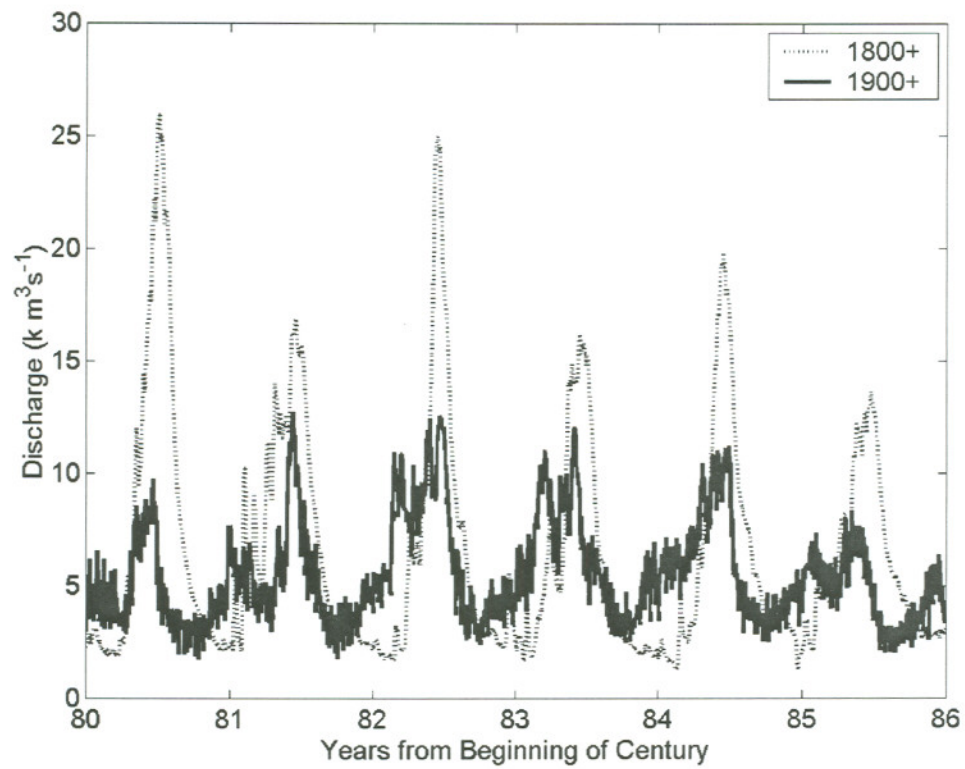


Fig. 2.2. Historical changes in river flow variability. Historical spring freshets were much larger than modern freshets. See also section 2.1.

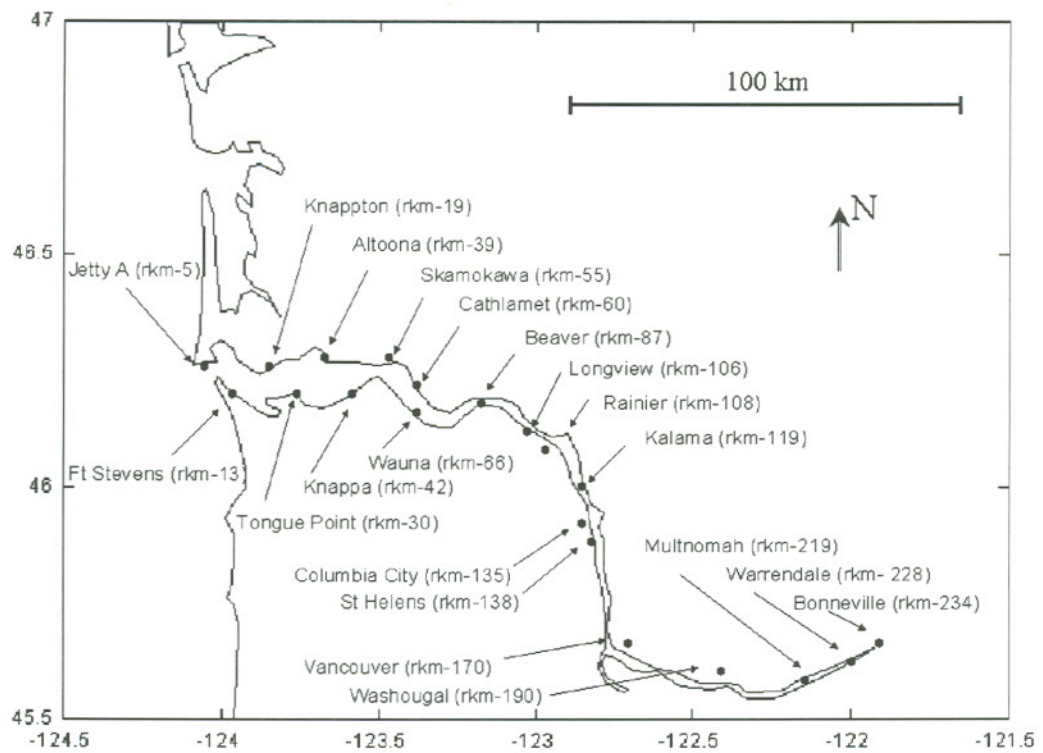


Fig. 2.3. Location map showing stations in the Lower Columbia River employed for tidal analysis.

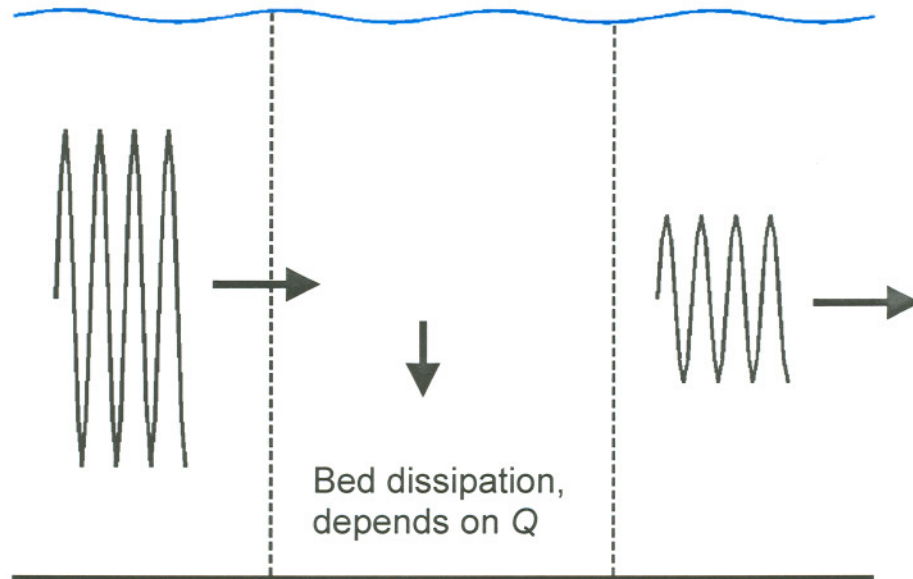


Fig 3.1. Conceptual model of a propagating tidal wave. Tidal energy dissipates due to the bedstress causing a decrease in tidal amplitude. The dissipation rate is dependent on the river discharge, the greater discharge values the greater the dissipation and the stronger is the tidal damping.

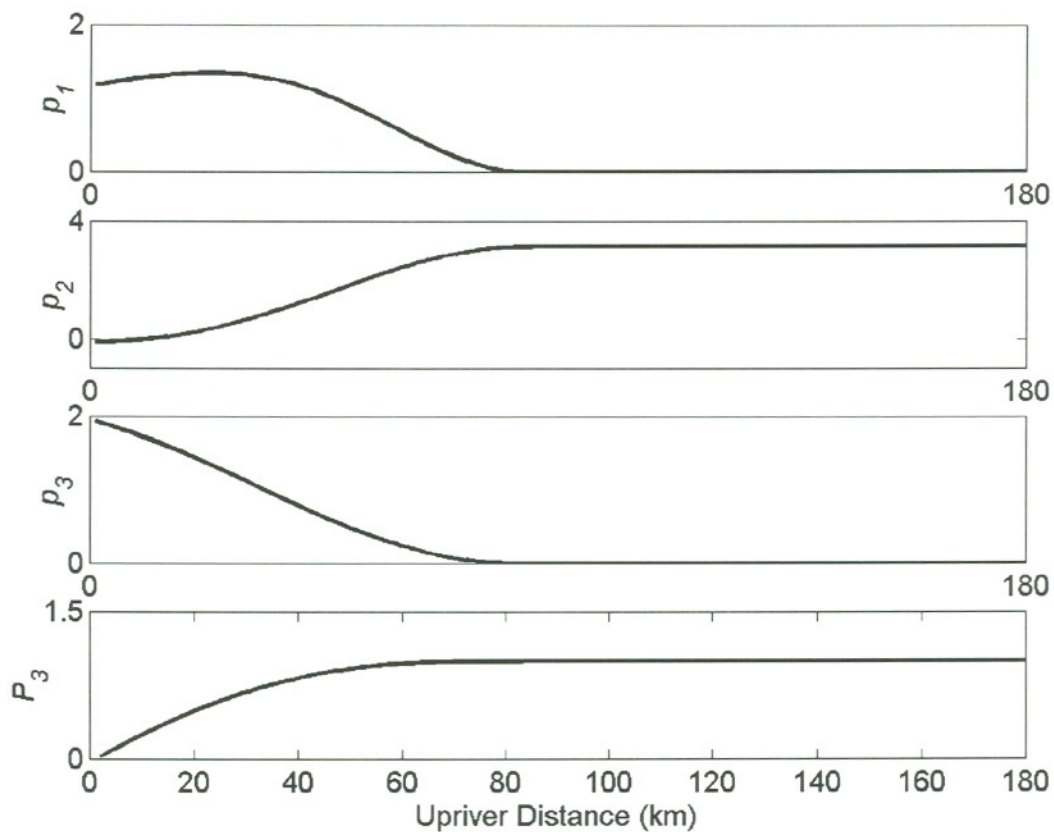


Fig. 3.2. Tschebyshev coefficients p_1 , p_2 , and p_3 and the integral P_3 (defined in section 5.2.2) as function of upriver distance. The following assumptions were made for this plot: current reversal occurs only seaward of Beaver, the ratio of tidal to river flow currents at the estuary entrance is 5, and tidal currents decrease linearly with x .

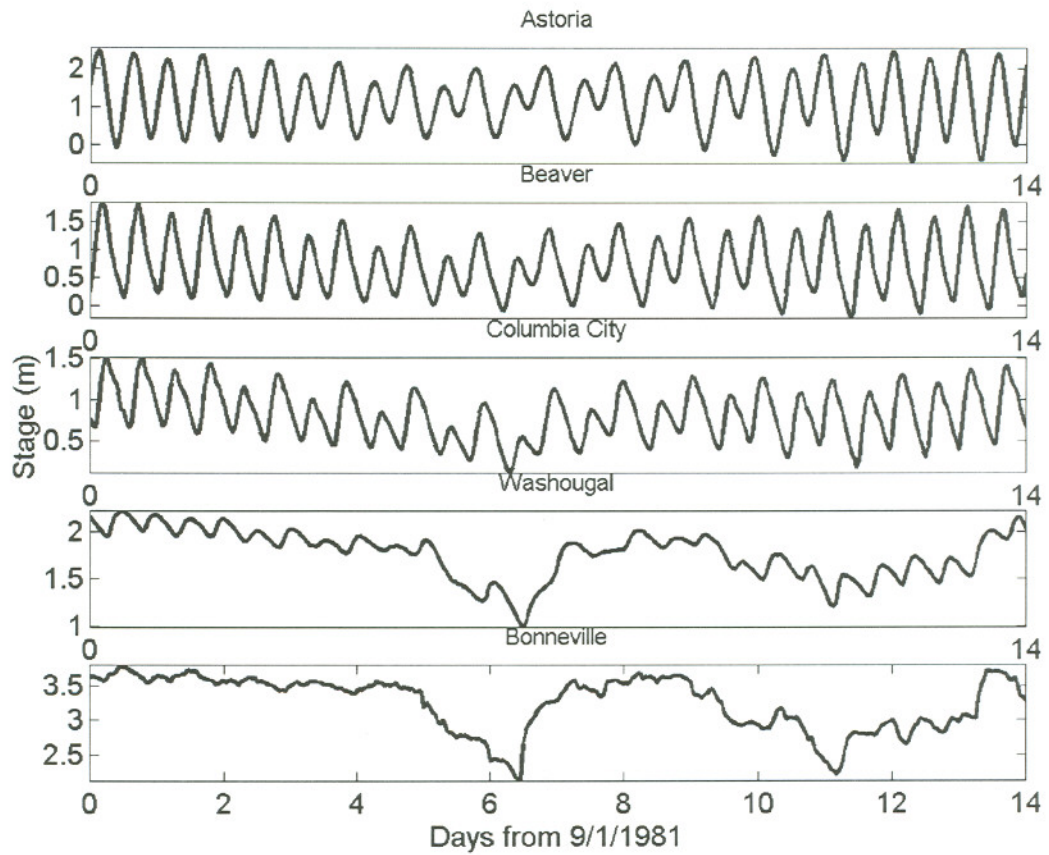


Fig. 5.1. Time series of surface elevation, illustrating damping and distortion of the tide, and the effects of power peaking at Bonneville. See also section 5.1.

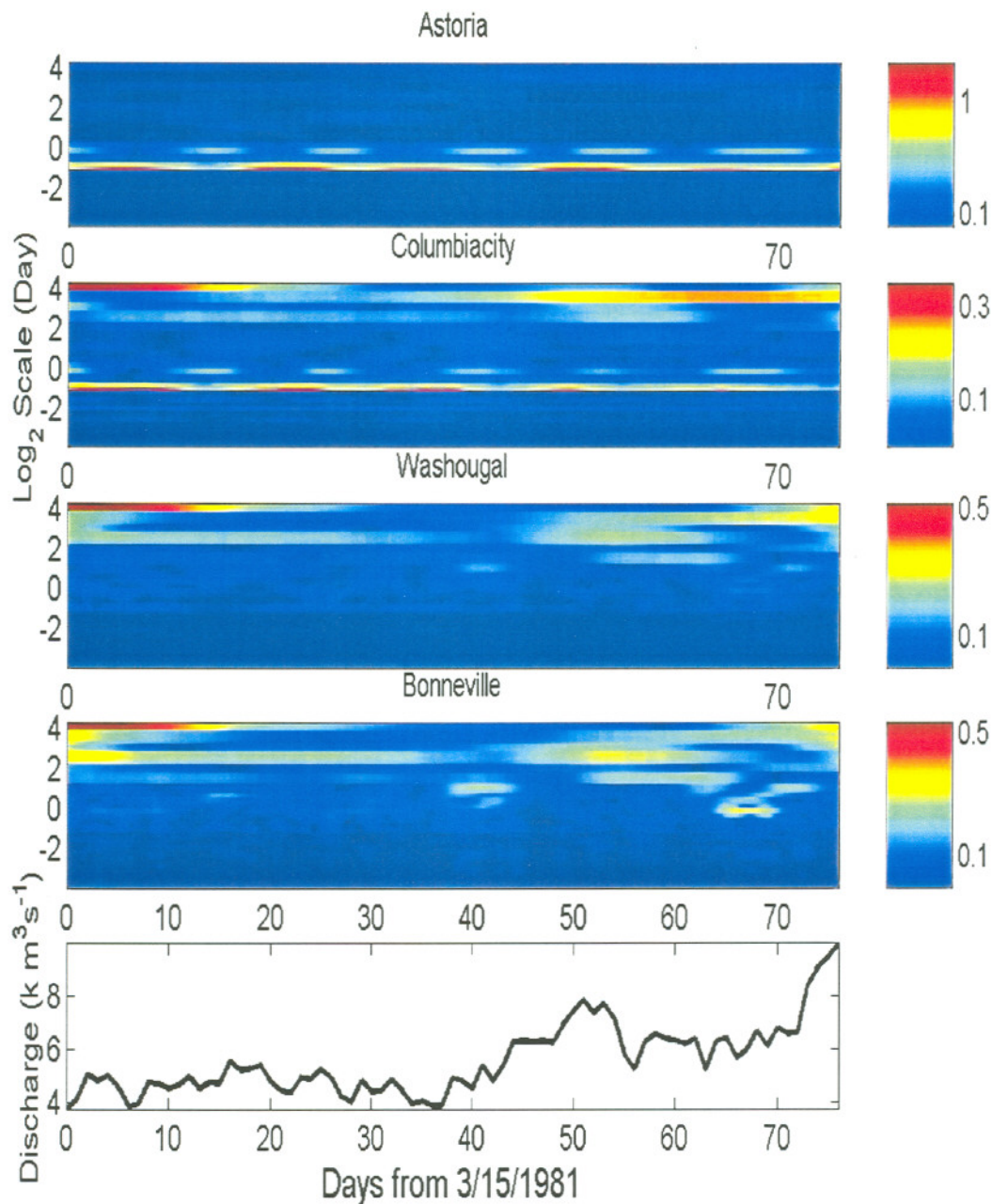


Fig. 5.2. Amplitude scaleograms illustrating the evolution of surface elevation amplitude at scales of 1/8 to 16 days. Colorbars show the amplitude of river stage scales in m. The tide changes its character from nearly stationary and band-limited at Astoria at rkm-29 (horizontal lines indicate wave processes) to non-stationary and broadband in the reach above Vancouver at rkm-171, where vertical "event cones" dominate the scalogram. See also section 5.1.

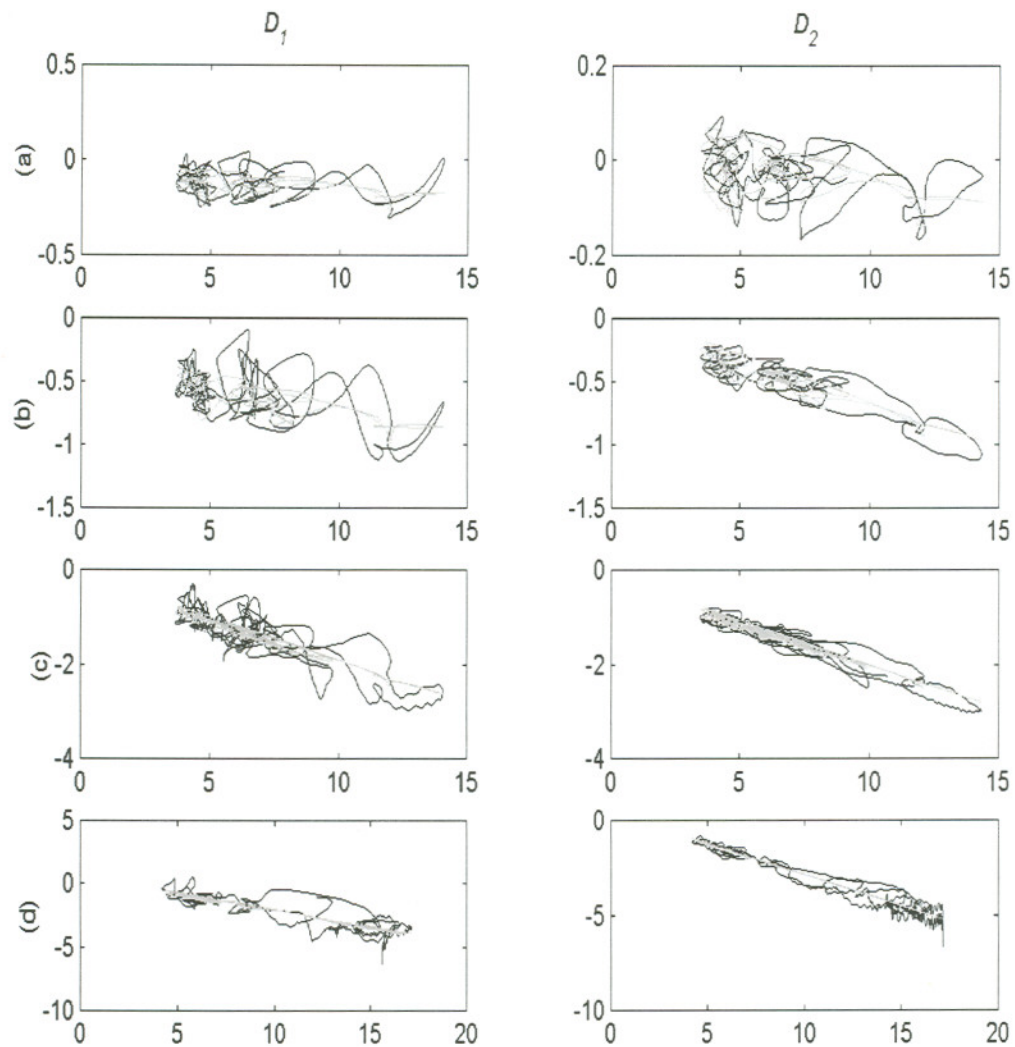


Fig. 5.3a. Observed (black) and modeled (gray) log-normalized tidal amplitudes for D_2 and D_1 versus river discharge ($\text{k m}^3 \text{s}^{-1}$) at the stations Altoona, Beaver, and Columbia City in 1981, (a), (b), and (c) respectively, and Vancouver in 1997 (d).

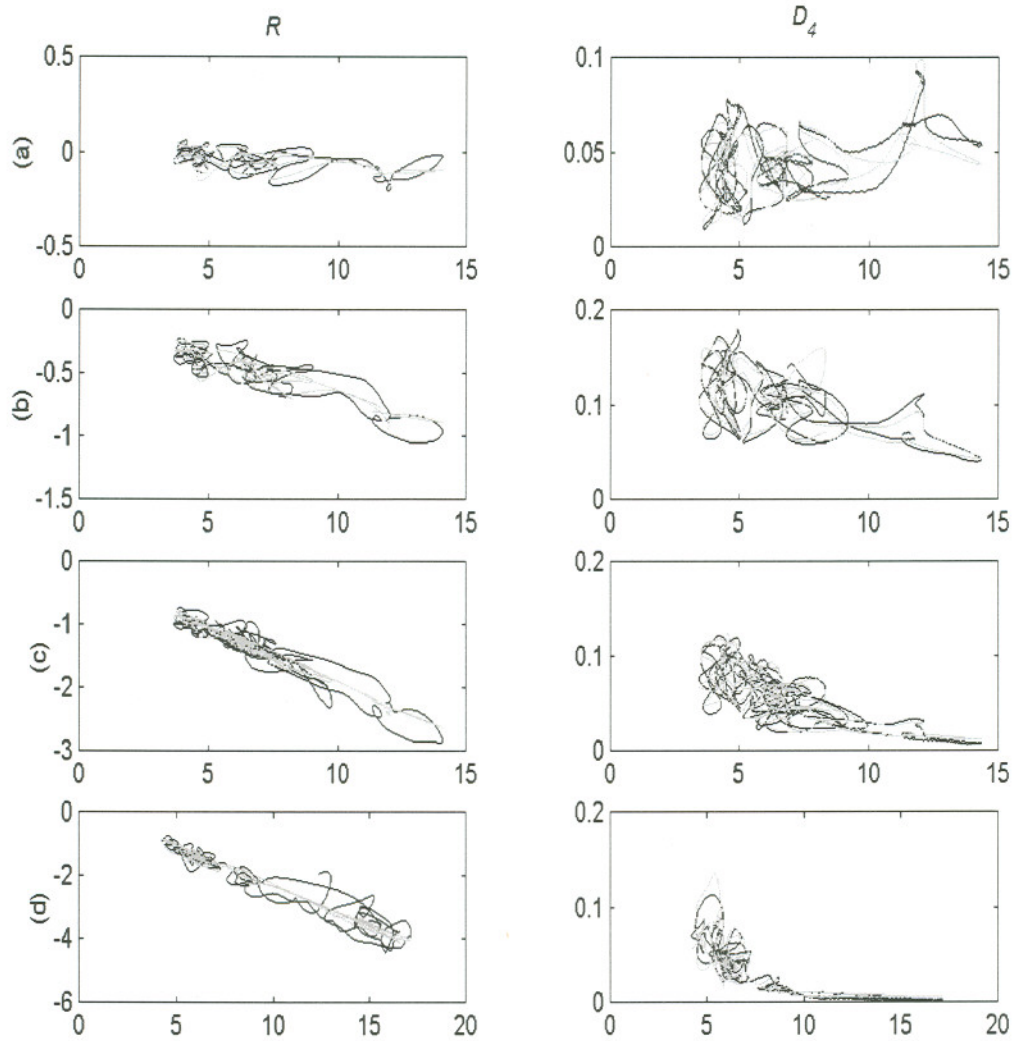


Fig. 5.3b. Observed (black) and modeled (gray) log-normalized tidal range R and tidal amplitude D_4 versus river discharge ($\text{k m}^3 \text{s}^{-1}$) at the stations Altoona, Beaver, and Columbia City in 1981, (a), (b), and (c) respectively, and Vancouver in 1997 (d).

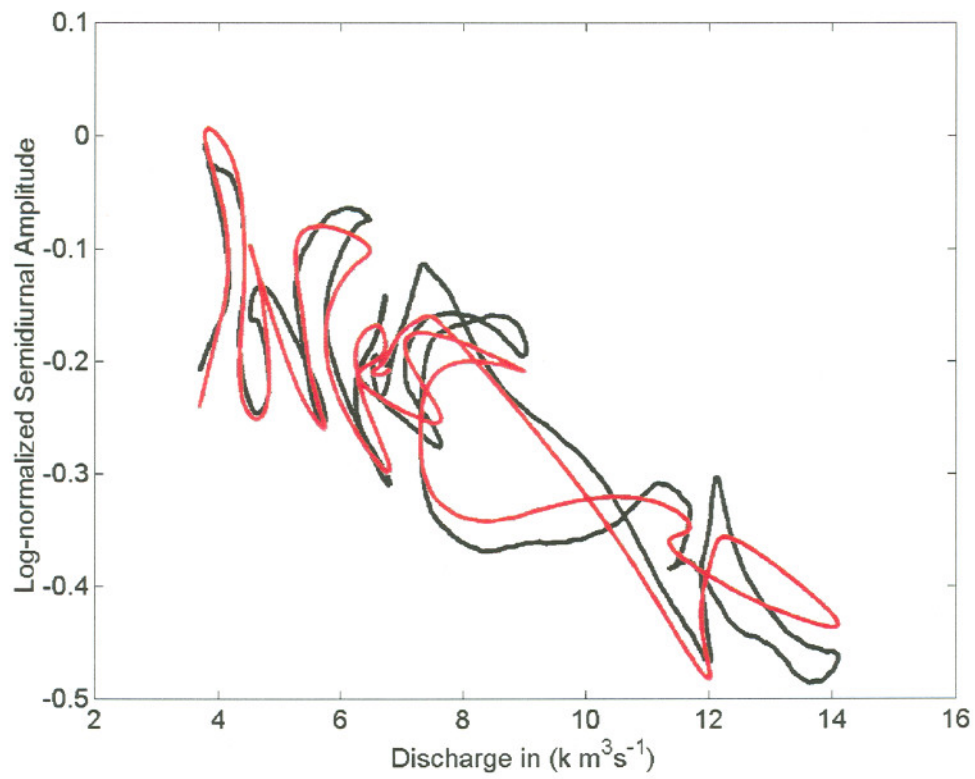


Fig. 5.3c. Log-normalized semi-diurnal tidal amplitude versus upriver distance at Cathlamet, rkm-60, in 1981.

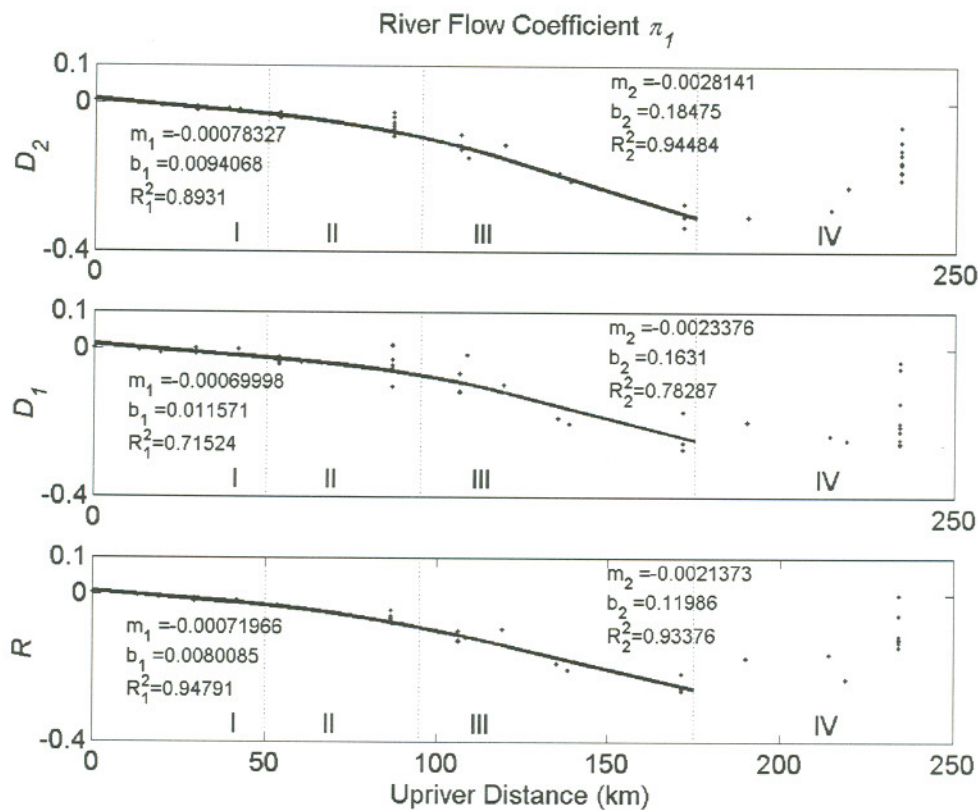


Fig. 5.4. The river flow coefficient π_1 as function of upriver distance for semidiurnal, diurnal, and tidal range amplitude. Each dot represents the coefficient determined for a particular station year. The curve shows a two step linear regression for the two reaches from Jetty A to Beaver (rkm-5 to 87) and from Beaver to Vancouver (rkm-87 to 171). In the transition region II the linear curves are connected with a cubic spline. The slope is m , y-intercept b , and R-square R^2 .

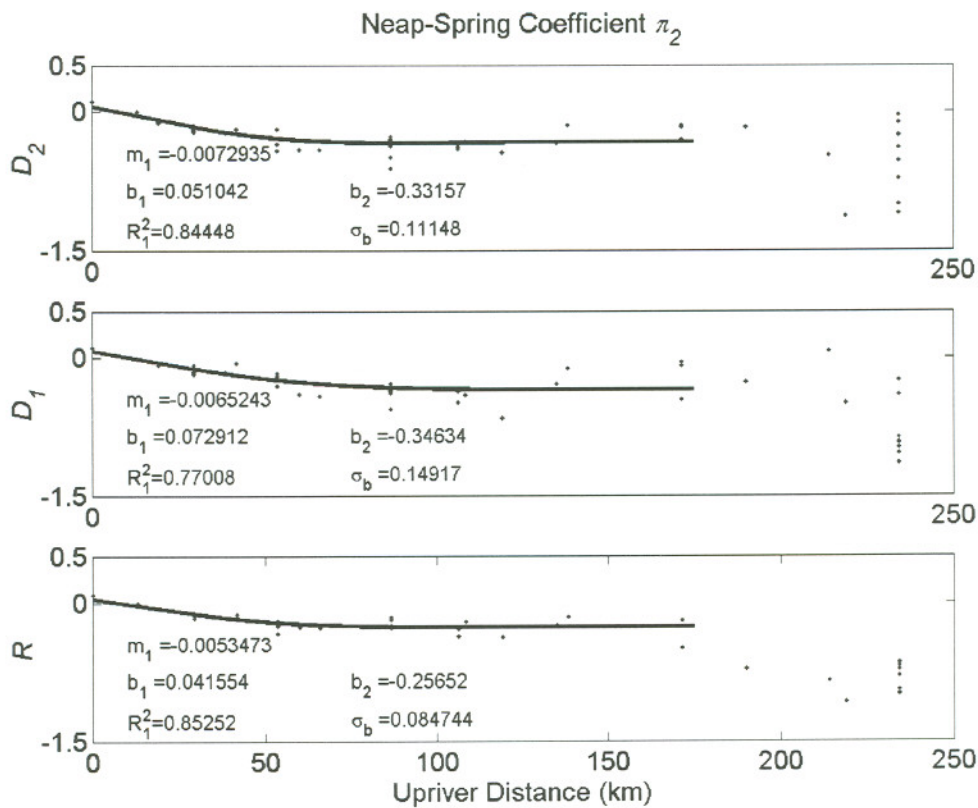


Fig. 5.5. The neap-spring coefficient π_2 as a function of upriver distance for semidiurnal, diurnal, and tidal range amplitude. Each dot represents the coefficient determined for a particular station year. The curve shows a linear regression for the reaches from rkm-5 to 50 and the average from rkm-50 to 171. In the transition region the linear curves are connected with a cubic spline. The slope is m , y-intercept b , and R-square R^2 . The standard deviation of b_2 is σ_b .

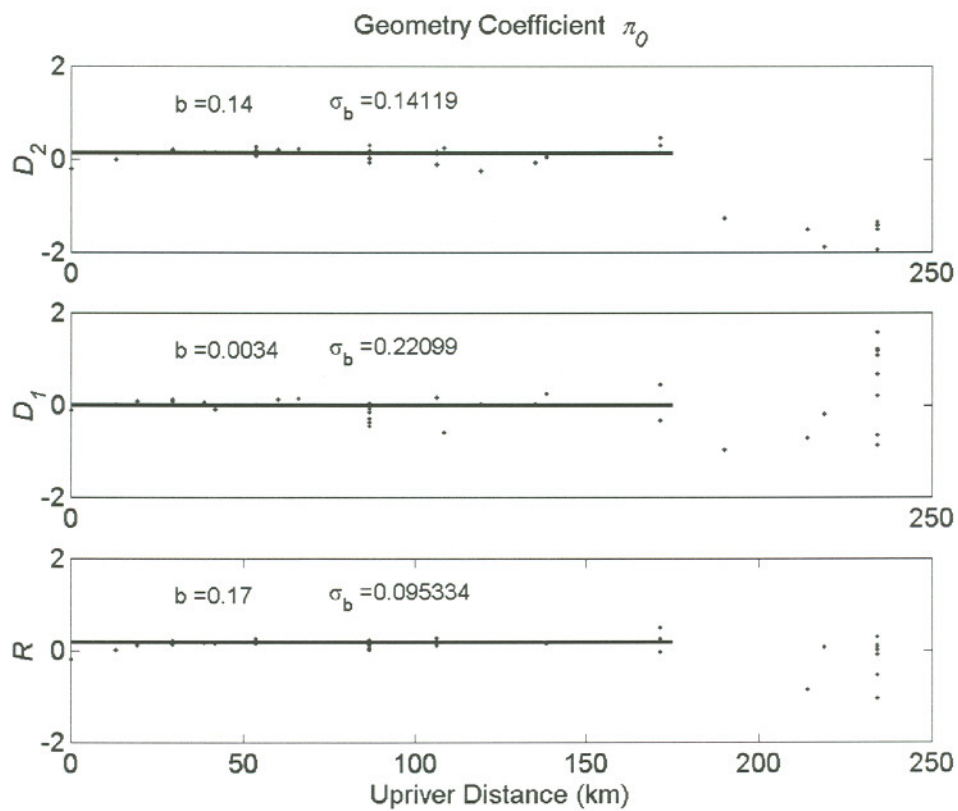


Fig. 5.6. The geometry coefficient π_0 as a function of upriver distance for semidiurnal, diurnal, and tidal range amplitude. The line shows the average b of the coefficients for rkm-5 to 171. The standard deviation of b is σ_b .

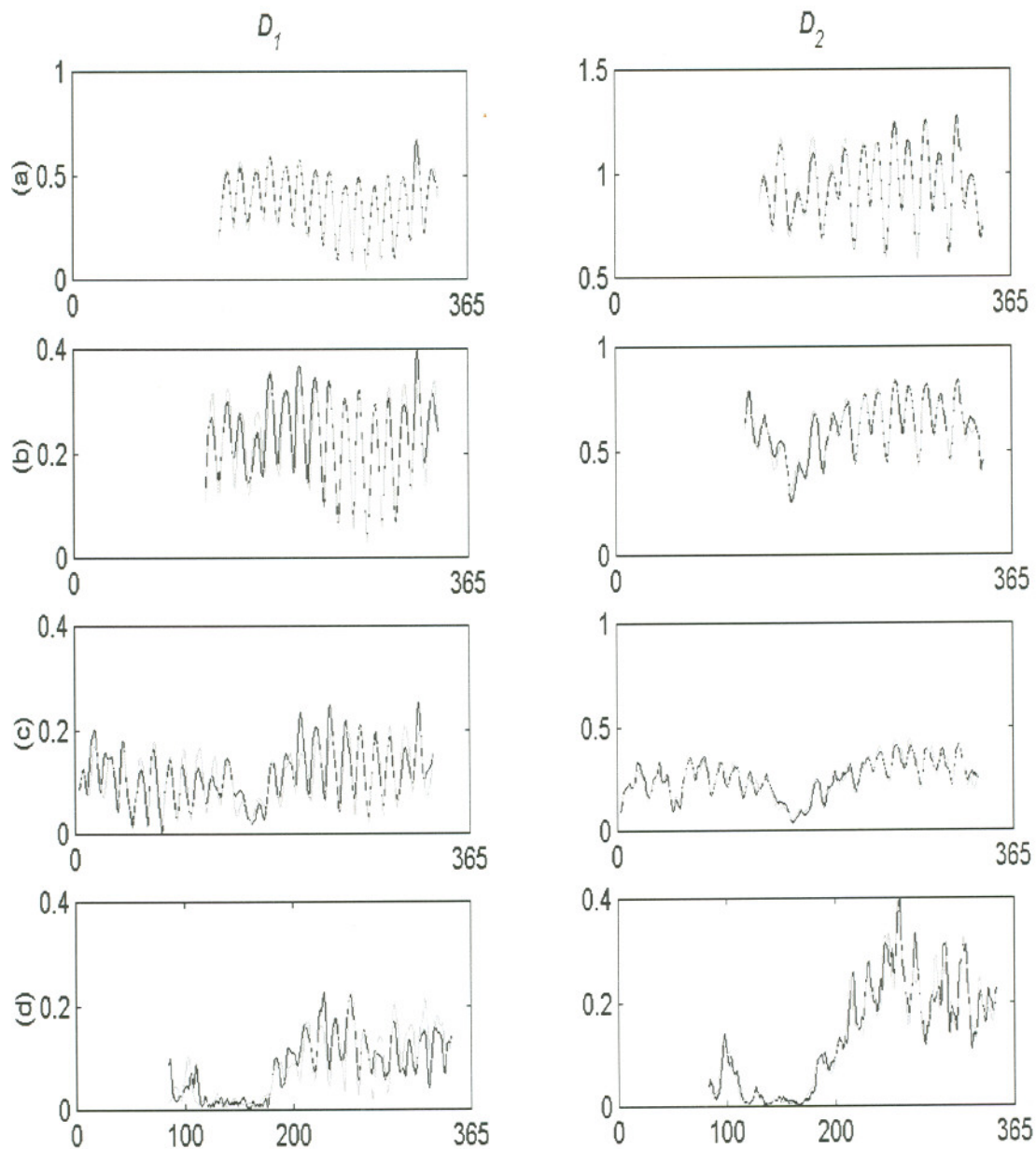


Fig. 5.7a. Observed (black) and modeled (gray) tidal amplitudes for D_2 and D_1 at the stations Altoona, Beaver, and Columbia City in 1981, (a), (b), and (c) respectively, and Vancouver in 1997 (d). The x-axes show days from January first.

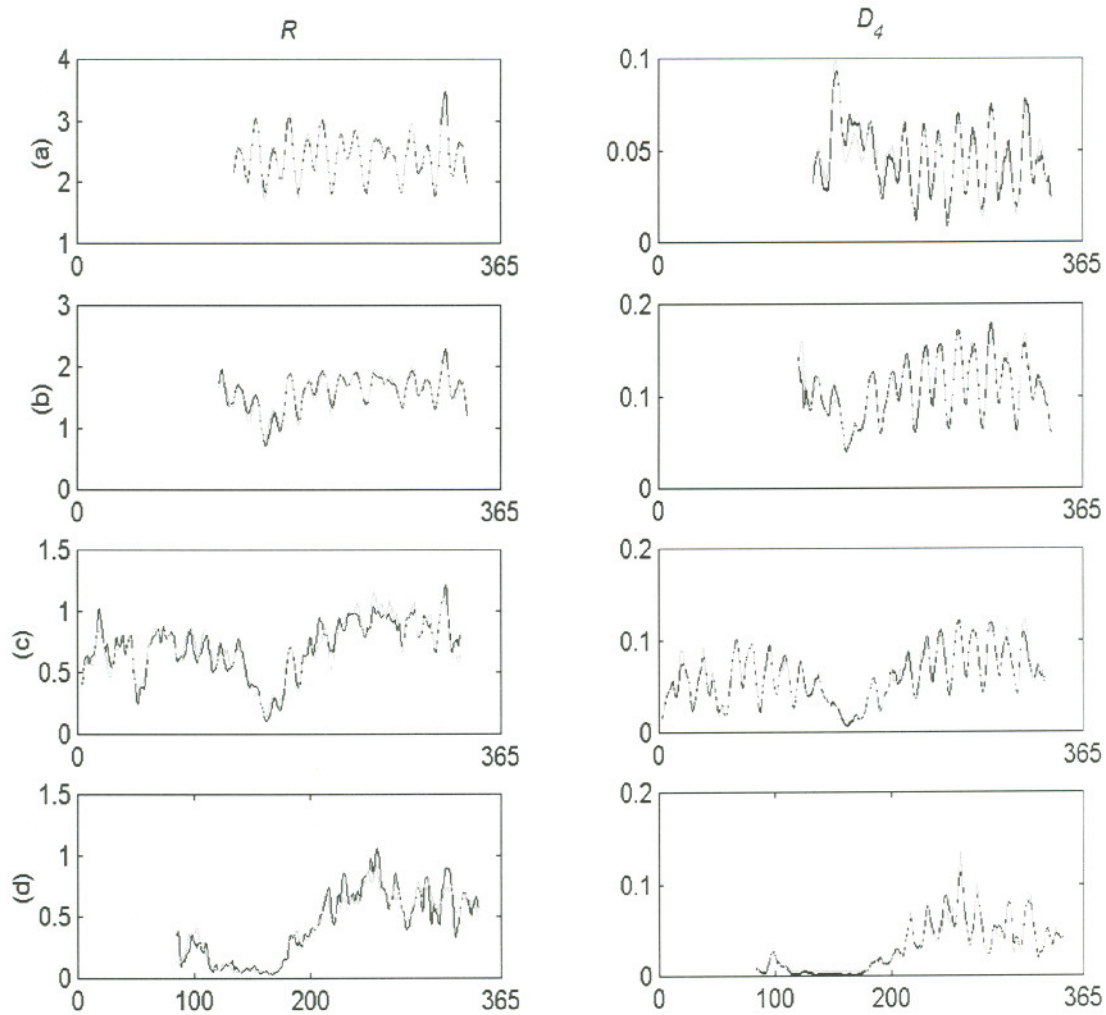


Fig. 5.7b. Observed (black) and modeled (gray) tidal amplitudes (in m) for R and D_4 at the stations Altoona, Beaver, and Columbia City in 1981, (a), (b), and (c) respectively, and Vancouver in 1997 (d). The x-axes show days from January first.

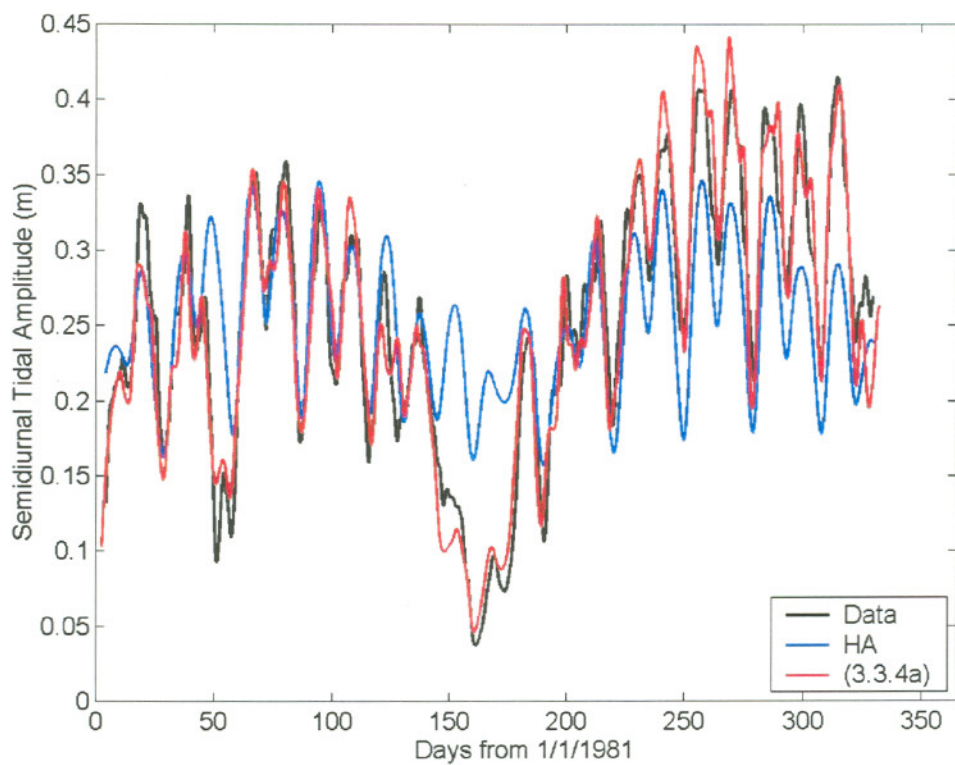


Fig. 5.8a. Observed semidiurnal tidal amplitude at Columbia City compared to predictions from HA and from (3.3.3a).

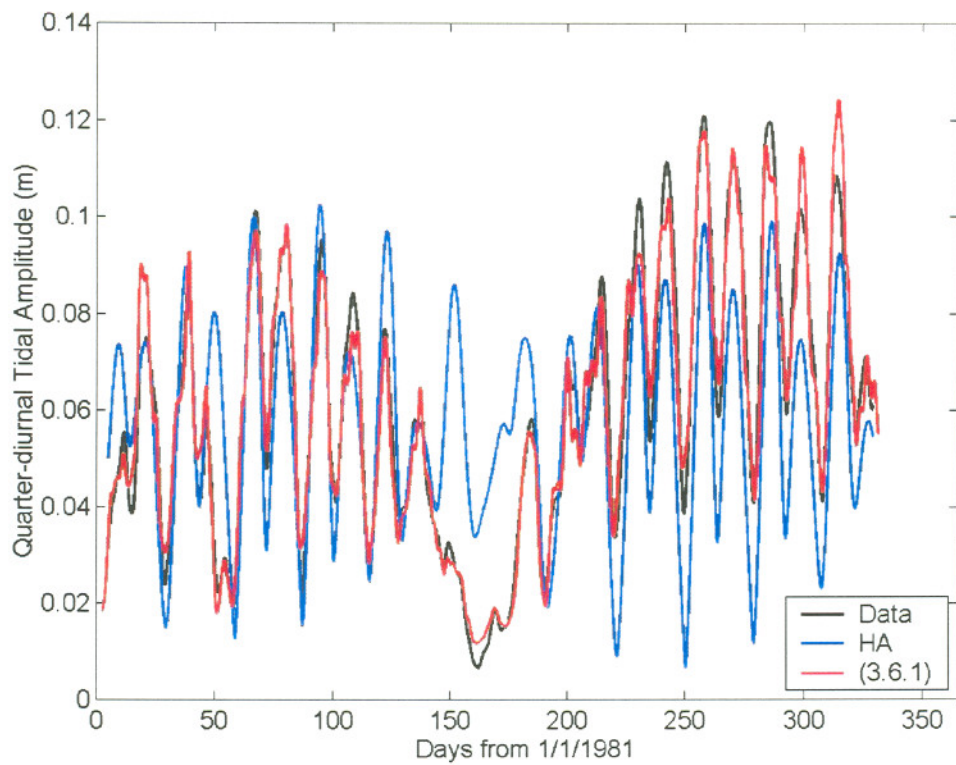


Fig. 5.8b. Observed quarter-diurnal tidal amplitude at Columbia City compared to predictions from HA and (3.6.1).

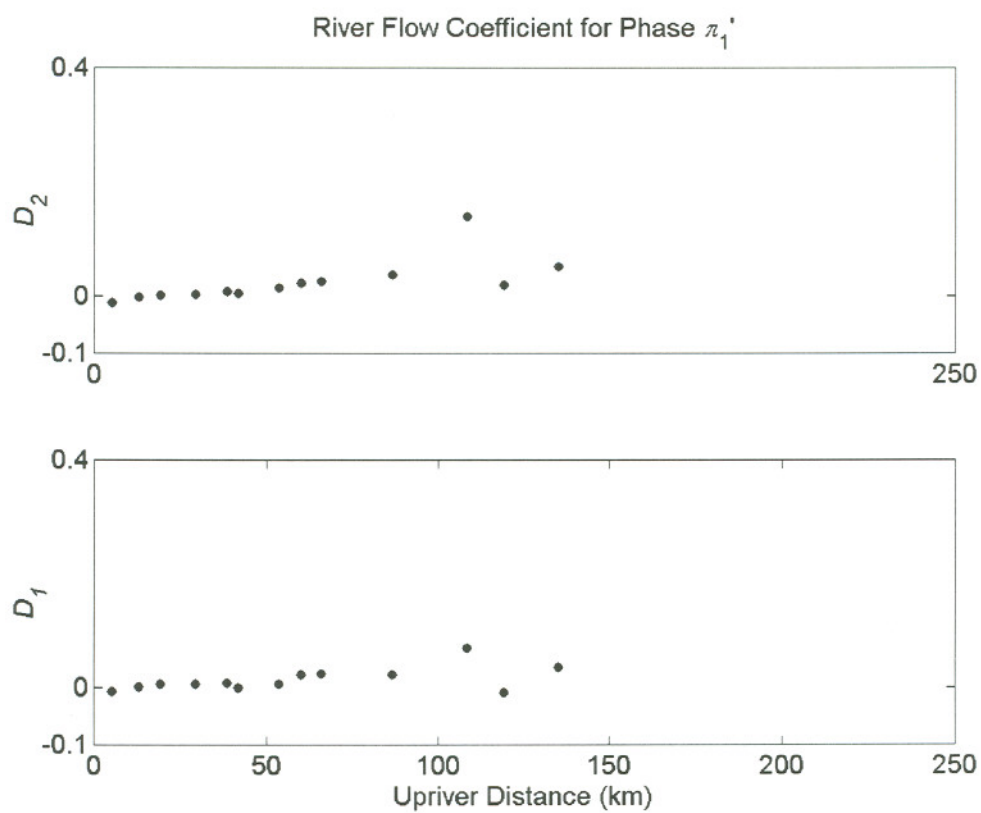


Fig. 5.9. Flow coefficient π_1' for the D_2 (upper panel) and D_1 (lower panel) phase in 1981.

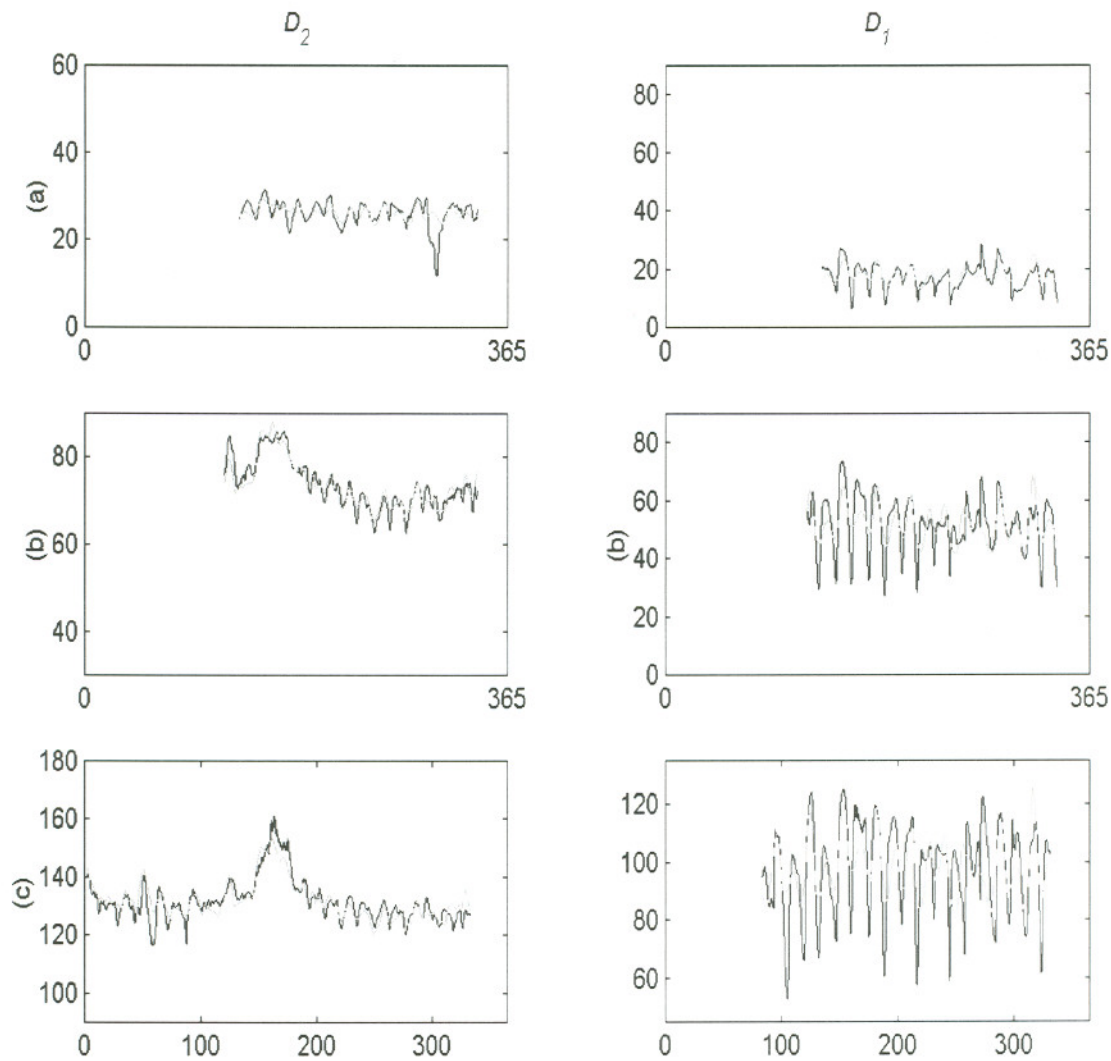


Fig. 5.11. Observed (black) and modeled (gray) D_2 and D_1 tidal phase differences (in $^\circ$) between reference station at Ft. Stevens and stations at Altoona, Beaver, and Columbia City in 1981, (a), (b), and (c) respectively. The x-axes show days from January first.

Appendices

Appendix A: Simplifications for regression model in section 3.4:

$$\begin{aligned}
 r &= \frac{1}{c_0} \sqrt{\frac{c_D U_s \omega}{2H\pi}} \left(p_1 + p_2 u_R + p_3 \left(3u_R^2 + \frac{1}{2} u_T^2 \right) \right)^{\frac{1}{2}} \\
 &\approx \frac{1}{c_0} \sqrt{\frac{c_D U_s \omega}{2H\pi}} \sqrt{p_2 u_R} \left(1 + \frac{p_3}{p_2} \left(3u_R + \frac{1}{2} \frac{u_T^2}{u_R} \right) \right)^{\frac{1}{2}} \\
 &\approx \frac{1}{c_0} \sqrt{\frac{c_D U_s \omega}{2H\pi}} \sqrt{p_2 u_R} \left(1 + \frac{3p_3}{2p_2} u_R + \frac{p_3}{4p_2} \frac{u_T^2}{u_R} \right) \\
 &\approx \frac{1}{c_0} \sqrt{\frac{c_D U_s \omega}{2H\pi}} \left(u_R \left(\sqrt{p_2} \sqrt{\frac{1}{u_R}} + \frac{3p_3}{2\sqrt{p_2}} \sqrt{u_R} \right) + \frac{p_3}{4p_2} \frac{u_T^2}{\sqrt{u_R}} \right) \\
 &\approx c_1' u_R + c_2' \frac{u_T^2}{\sqrt{u_R}},
 \end{aligned}$$

with

$$c_1' = \frac{1}{c_0} \sqrt{\frac{c_D U_s \omega}{2H\pi}} \left(\sqrt{p_2} \sqrt{\frac{1}{u_R}} + \frac{3p_3}{2\sqrt{p_2}} \sqrt{u_R} \right) \quad \text{and}$$

$$c_2' = \frac{1}{c_0} \sqrt{\frac{c_D U_s \omega}{2H\pi}} \frac{p_3}{4p_2}$$

Appendix B: Development of first-order relationship for Z_R in section 3.5:

$$\begin{aligned}
 Z_R(x) &\cong \log\left(\frac{\exp(\bar{\pi}_{D2} \bullet \bar{X}^T) + f \exp(\bar{\pi}_{D1} \bullet \bar{X}^T)}{1 + f}\right) \\
 &= \log\left(\exp(\bar{\pi}_{D2} \bullet \bar{X}^T) [1 + f \exp(\{\bar{\pi}_{D1} - \bar{\pi}_{D2}\} \bullet \bar{X}^T)]\right) - \log(1 + f) \\
 &\cong \bar{\pi}_{D2} \bullet \bar{X}^T + \log\left(1 + f \exp(\{\bar{\pi}_{D1} - \bar{\pi}_{D2}\} \bullet \bar{X}^T)\right) - f \\
 &\cong \bar{\pi}_{D2} \bullet \bar{X}^T + f \exp(\{\bar{\pi}_{D1} - \bar{\pi}_{D2}\} \bullet \bar{X}^T) - f \\
 &\cong \bar{\pi}_{D2} \bullet \bar{X}^T + f(1 + \{\bar{\pi}_{D1} - \bar{\pi}_{D2}\} \bullet \bar{X}^T) - f \\
 &\cong ((1 - f)\bar{\pi}_{D2} + f\bar{\pi}_{D1}) \bullet \bar{X}^T
 \end{aligned}$$

Appendix C: Note on Error Analyses

Definition of rms (root-mean-square) error

If $\{y_i\}_{i=1\dots n}$ is a data set of n points y_i , and \hat{y}_i is the modeled value of y_i , and the model has k degrees of freedom, we define the root-mean-squared error, or short rms, as:

$$\text{rms} = \frac{1}{(n-k)} \sqrt{\sum_{i=1}^n (y_i - \hat{y}_i)^2}$$

Definition of error averaged over all station-years

If $\{\text{rms}_i\}_{i=1\dots N}$ is a set of N rms errors rms_i for a station-year of data with n_i data points, and N is the total number of station-years, the error averaged over all station-years σ is defined as:

$$\sigma = \sum_{i=1}^N \frac{n_i}{M} \text{rms}_i, \quad \text{where } M = \sum_{i=1}^N n_i$$

Model Bias

Averaged over all stations, the modeled amplitudes are underestimated by 0.9%, 3.0%, and 0.3% for D_2 , D_1 , and R respectively. It is likely that a bias towards smaller numbers arises from the regression analysis in log-space. The error due to log-space regression can be intuitively understood when averaging the number 1, 10, and 100: the

arithmetic average is 37, while the average in log space is 10 ($=10^{(1+2+3)/3}$). The model error, however, obscures this interpretation (Figs. Ap.1-Ap.3, Table 4). If the average of the ratio of observed amplitudes versus modeled deviates much from 1.0, the standard deviation of this ratio also increases (Fig. Ap.1a-Ap.3a), so that a bias is not statistically significant. The maximum error of underestimation for a station-year is on average 0.06m, 0.08m, and 0.11m for D_2 , D_1 , R , respectively.

The maximum error of overestimation for a station-year is on average -0.09m, -0.05m, and -0.07m for D_2 , D_1 , R , respectively. Maximal errors, however, vary considerably with a particular station year (Fig. Ap.1b-Ap.3b).

Scatter of Coefficients

We found that the scatter of the coefficients (see Table 5) is dependent on the range of river discharge used for the determination of coefficient for a particular station-year. For, example the flow coefficient π_1 at Beaver is on average for each year -0.057 with a standard deviation of 0.020. If the low discharge station-years 1992 and 1994 are excluded, which have average flow values of 5.3 and 5.2 km^3s^{-1} , respectively, during the analysis period, and a flow standard deviation of 1.1 and 0.9 km^3s^{-1} , respectively, the coefficient π_1 is -0.064 and its standard deviation decreases to 0.016. Flows for the station-years at Beaver without the years 1992 and 1994 average to 8.2 km^3s^{-1} with an average standard deviation of 2.7 km^3s^{-1} . Thus, π_1 at Beaver is significantly less scattered if it is determined with a great flow range. This makes sense, because tidal damping through river flow is a negative-exponential process, so that the flow must vary over a certain range, before tidal amplitude damping becomes a measurable effect.

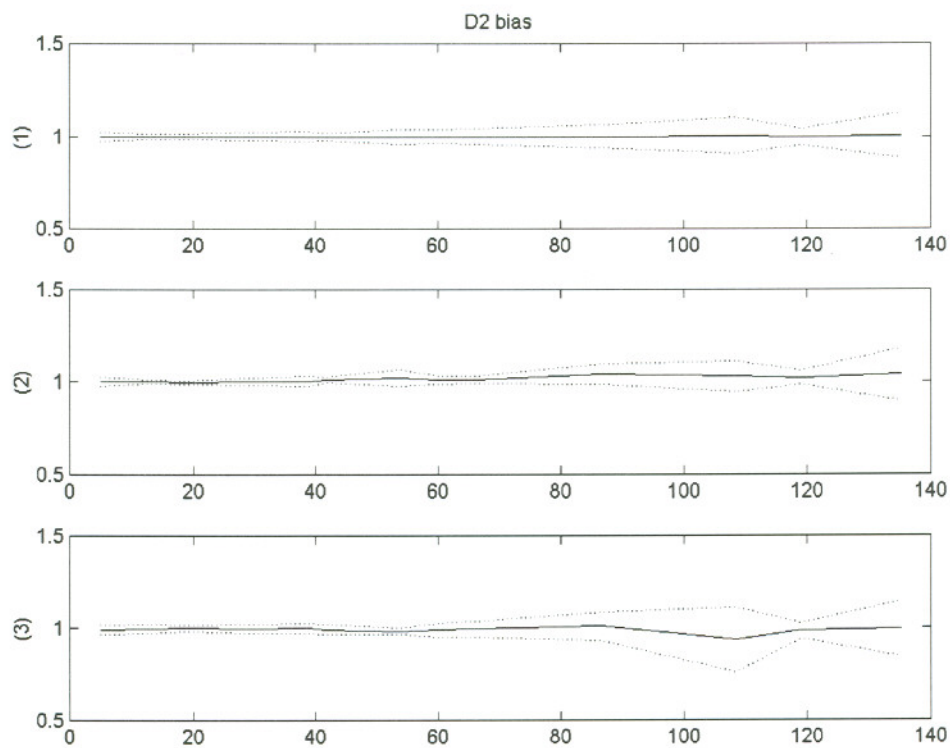
Figures for Appendix C

Fig. Ap.1a. Ratio of observed 1981 D_2 amplitudes to modeled (y-axis, unit-less) versus upriver distance (x-axis, in km), (1) averaged over all time points, (2) averaged over the neap-tide trough, and (3) averaged over spring-tide crest. Plus/minus one standard deviation of these ratios is shown in dotted lines.

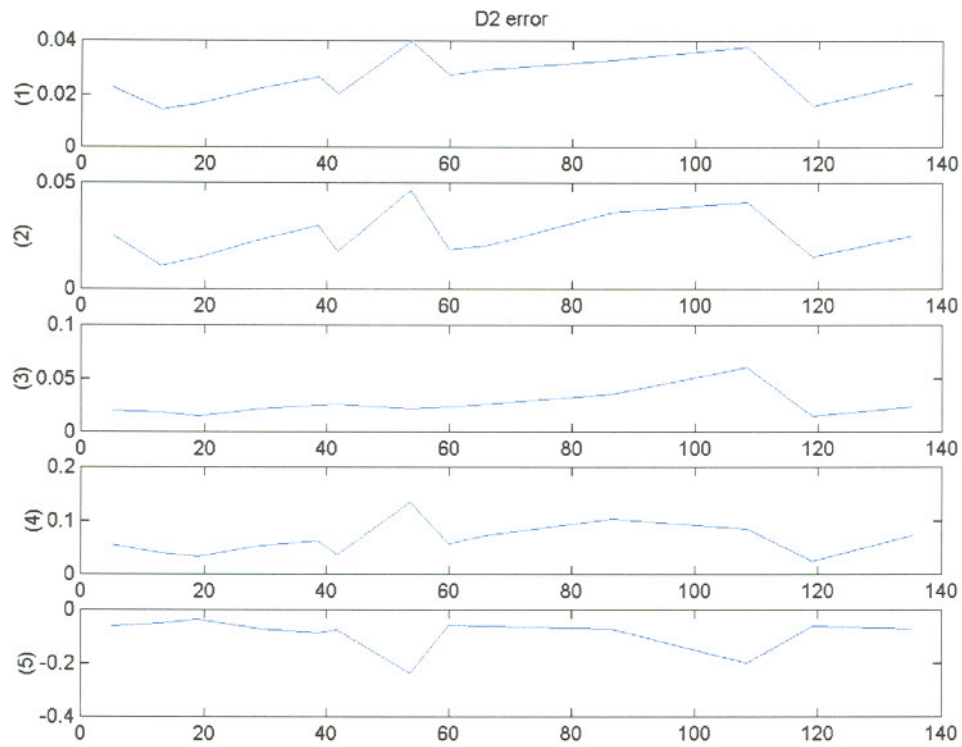


Fig. Ap.1b. D_2 amplitude model rms error (y-axis, in m) for each station in 1981 versus upriver distance (x-axis, in km) for (1) whole station-year, (2) troughs, and (3) crests. Maximal model error of (4) underestimation and (5) overestimation (y-axis, in m) versus upriver location (x-axis, in km).

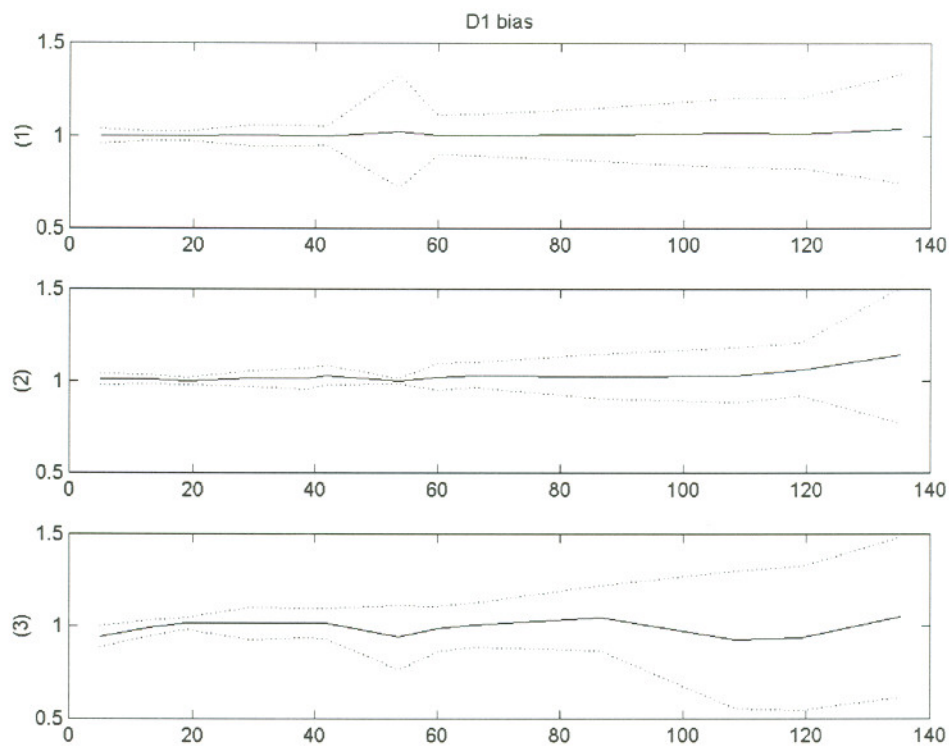


Fig. Ap.2a. Ratio of observed 1981 D_1 amplitudes to modeled (y-axis, unit-less) versus upriver distance (x-axis, in km), (1) averaged over all time points, (2) averaged over the neap-tide trough, and (3) averaged over spring-tide crest. Plus/minus one standard deviation of these ratios is shown in dotted lines.

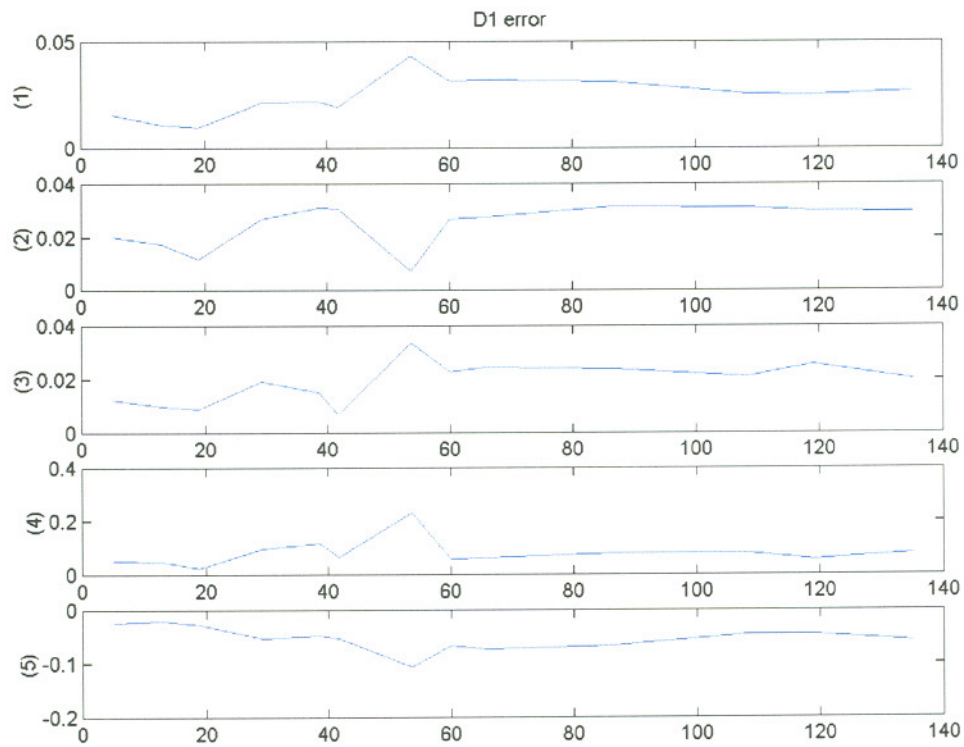


Fig. Ap.2b. D_1 amplitude model rms error (y-axis, in m) for each station in 1981 versus upriver distance (x-axis, in km) for (1) whole station-year, (2) troughs, and (3) crests. Maximal model error of (4) underestimation and (5) overestimation (y-axis, in m) versus upriver location (x-axis, in km).

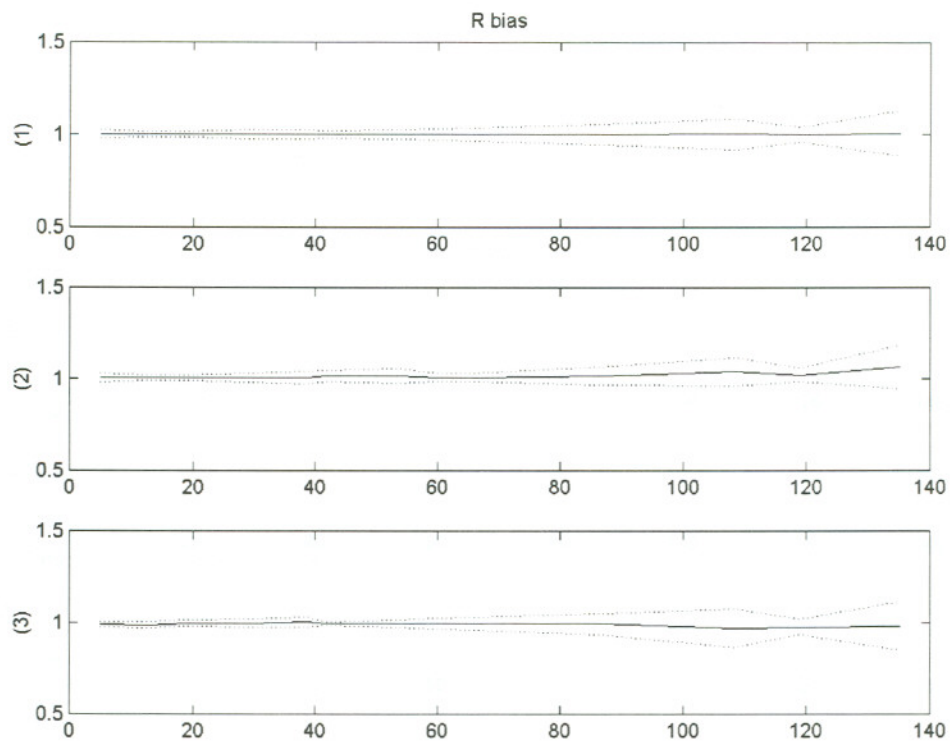


Fig. Ap.3. a. Ratio of observed 1981 R amplitudes to modeled (y-axis, unit-less) versus upriver distance (x-axis, in km), (1) averaged over all time points, (2) averaged over the neap-tide trough, and (3) averaged over spring-tide crest. Plus/minus one standard deviation of these ratios is shown in dotted lines.

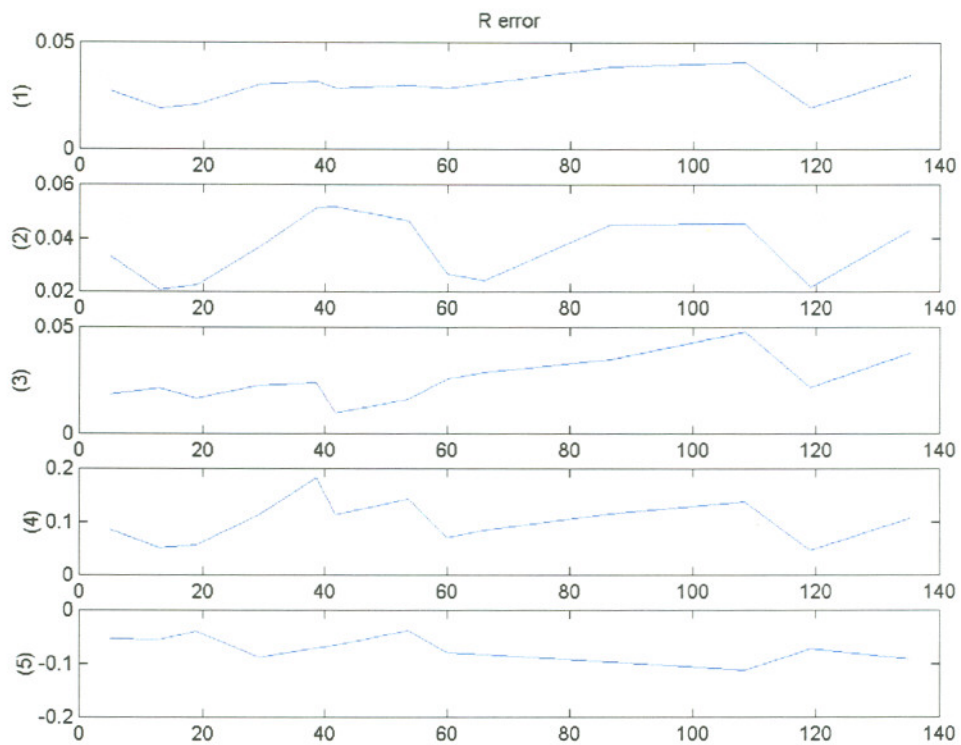


Fig. Ap.3b. *R* amplitude model rms error (y-axis, in m) for each station in 1981 versus upriver distance (x-axis, in km) for (1) whole station-year, (2) troughs, and (3) crests. Maximal model error of (4) underestimation and (5) overestimation (y-axis, in m) versus upriver location (x-axis, in km).

Biographical Sketch

Tobias Kukulka was born on September 22nd, 1976, in Berlin, Germany. He received his Vordiplom in Physics from the Freie Universität Berlin (Germany) in 1998. Since 2000, he has been working toward a M.S. degree in Environmental Science and Engineering under the supervision of David A. Jay at the OGI School of Science & Engineering at OHSU. His research interests include estuarine processes, waves and tides, air-sea interactions, and data analysis methods.